Hindawi
Journal of Chemistry
Volume 2023, Article ID 5540233, 21 pages
https://doi.org/10.1155/2023/5540233

Research Article

Rapid and Efficient Degradation of Ceftiofur Sodium by 5,6-Dimethylbenzimidazole-Modified ZIF(Fe/Co)$_x$@CNF Nanocomposites

Hao Fu,[1] Aotian Gu,[1] Peng Wang,[1] Chunhui Gong,[1] Zhiying Li,[1] Kai Chen,[2] and Yi Yang[1,2]

[1]*Jiangsu Key Laboratory of Chemical Pollution Control and Resources Reuse, School of Environmental and Biological Engineering, Nanjing University of Science and Technology, Nanjing 210094, China*
[2]*Collaborative Innovation Center of Atmospheric Environment and Equipment Technology, Jiangsu Key Laboratory of Atmospheric Environment Monitoring and Pollution Control (AEMPC), Nanjing University of Information Science & Technology, Nanjing 210044, China*

Correspondence should be addressed to Yi Yang; yangyi@njust.edu.cn

Received 11 January 2023; Revised 12 March 2023; Accepted 21 April 2023; Published 19 May 2023

Academic Editor: Balasubramani Ravindran

The exploration of transforming various metals as metal sources into metal organic frameworks (MOFs) has attracted considerable attention in recent years. This study used triethylamine and 5,6-dimethylbenzimidazole (DMBIM) to modify the iron-doped cobalt zeolite imidazole framework on carbon fiber structure. The results showed that the ZIF(Fe/Co)$_{1.25}$@CNF exhibited high CEF removal efficiency that over 97% of ceftiofur sodium (CEF) was removed within 10 min, which was significantly higher than that of the common ZIF-67 materials. Compared with other ZIF-67 composites, ZIF(Fe/Co)$_x$@CNF has a larger specific surface area, resulting in a larger contact area and more active sites during the reaction. After the introduction of DMBIM, the ZIF(Fe/Co)$_{1.25}$@CNF not only easily separated from the solution but also enhanced the hydrophobicity, which provided higher catalytic stability and catalytic performance. In addition, the effects of different catalyst ratios, pollutant concentrations, solution pH, and different radicals (•OH, $SO_4^{\bullet-}$, $^1O_2$) on the activation of peroxymonosulfate (PMS) were investigated. The mechanism of degradation was elucidated by electron paramagnetic resonance experiments. This study provides a new perspective for the preparation of high-performance MOF catalysts with excellent catalytic performance and may facilitate the application of MOF materials in more practical situations.

1. Introduction

The application of antibiotics as the most commonly prescribed drugs in modern medicine has long been used for the prevention and treatment of infectious diseases in humans and animals. Globally, most countries face water quality problems, and even groundwater that is considered safe can become contaminated with CEF [1, 2]. In this context, a range of antibiotics are eventually released into the environment due to their high complexity, highly stable biological activity, and indiscriminate use, resulting in persistent ecological pollution. As a persistent pollutant in the environment, antibiotics are mainly derived from wastewater produced by households, hospitals, aquaculture, and livestock and pharmaceutical industries [3] and are discharged to wastewater treatment plants, either through drainage networks or surface runoff, and conventional wastewater treatment plants are not specifically designed to remove antibiotics, so these molecules are released directly into the host environment [4–6].

Of the various classes of antibiotics, β-lactams (BLA), fluoroquinolones (FQs), tetracyclines (TCs), macrolides (MLs), and sulfonamides (SAs) are the most commonly prescribed antibiotics. Penicillins and cephalosporins are jointly the second most popular antibacterial drugs in China since 2013 [7]. Ceftiofur sodium (CEF), a third-generation

animal-specific cephalosporin antibiotic, is widely used in clinical practice to control animal diseases and is one of the most commonly used antibiotics in animal husbandry to control infections and improve animal production [8–13]. The widespread use of CEF induces the growth of drug-resistant microorganisms due to its unique chemical structure [10]. This β-lactam-based antibiotic inhibits bacterial cell wall synthesis and is highly water soluble, accumulates in the environment, and enters the ecological water cycle, causing pollution of the aquatic environment [10, 14]. Therefore, the removal of ceftiofur sodium from water bodies has become one of the urgent problems to be solved.

Coagulation, membrane separation, adsorption, and biodegradation are some of the main approaches for CEF removal in wastewater treatment processes. However, conventional methods such as biodegradation as well as adsorption have not been widely used due to their low removal efficiency and high operating costs [15–17]. Advanced oxidation processes (AOPs) can degrade antibiotics or convert them to smaller molecules, thereby reducing the inhibitory effect of antibiotics on microorganisms and thus improving their biodegradability and removal rates [18, 19]. Presently, a part of advanced oxidation technology has been applied in wastewater treatment, and the overall treatment effect was found to be satisfactory. Specifically, it has significant advantages in organic wastewater treatment but requires some specific conditions to effectively achieve excellent oxidation performance. Different types of wastewater in combination with treatment conditions tend to affect the generation of free radicals, which will negatively impact the pollutant removal efficiency and affect the effluent quality. Therefore, activated peroxymonosulfate advanced oxidation technology has attracted extensive attention [20, 21]. In sulfate (SO_4^{-})-based advanced oxidation, highly reactive sulfate radicals ($SO_4^{\bullet-}$) are generated by cleaving peroxide bonds in the persulfate molecule through energy and electron transfer reactions. The advanced oxidation of peroxymonosulfate has a higher yield of radical formation compared to other advanced oxidation techniques [22, 23], and in terms of radical oxidation capacity, $SO_4^{\bullet-}$ has a redox potential (2.5–3.1 V) equal to or even higher than that of •OH (2.8 V), and $SO_4^{\bullet-}$ is applicable to a higher pH range, thus showing a more powerful ability in degrading organic compounds [24, 25]. In addition, $SO_4^{\bullet-}$ has a longer half-life relative to •OH, making $SO_4^{\bullet-}$ a more stable mass transfer effect and easier contact with the target compounds [26]; it is also more selective than •OH for organic compounds with unsaturated bonds or aromatic electrons [26].

Metal organic frameworks (MOFs) are crystalline porous materials with a periodic network structure formed by self-assembly of inorganic metal centers and organic ligands connected by an external backbone. There are numerous studies reported so far on the activation of PMS by MOFs. Compared with conventional catalysts, MOFs have comparatively adjustable pore structure and ultrahigh specific surface area, exhibiting superior catalytic performance and good application prospects. Several studies have prepared bimetallic MOFs by adding a second metal to the MOFs backbone, and these bimetallic MOFs exhibit higher catalytic activity compared to monometallic MOFs [27, 28]. For example, Gu et al. successfully synthesized bimetallic MOFs (M/Z_x) consisting of an ordered ZIF-67 (Co) shell and MIL-101 (Fe) core by a simple method, which exhibited excellent PMS activation performance and could achieve 90% 2-cp (100 mg/L) removal within 10 min [29].

CNFs have also been recently reported as a matrix for the preparation of MOFs composites [30–32]. Compared with pure MOFs, the agglomeration of MOFs can be alleviated when MOFs are loaded on fibrous materials [33]. Previously, Feng et al. synthesized a new type of ZIF-67@PCF composite using hollow porous carbon fibers as a precursor to limit the growth and aggregation of MOFs and promote mass transfer, which exhibited excellent electrocatalytic activity [30]. In addition, carbon fiber itself has been used as an effective green catalyst to activate peroxymonosulfate (PMS) for the degradation of aqueous organic pollutants [32]. Yang et al. used activated carbon fiber (ACF) as a catalyst to activate PMS for the degradation of aqueous organic pollutants and showed that a very low dose of ACF ($0.3\ g{\cdot}L^{-1}$) could effectively activate PMS to eliminate acidic Orange 7 (AO7) [34]. The composite material, on the other hand, also facilitates the separation of the catalyst from the reaction solution during the degradation process, solving an important challenge in practical applications. In summary, previous studies have demonstrated that MOFs-based AOPs are poised to play an important role in the elimination of refractory organic pollutants. However, most of the reported catalysts based on MOFs or MOFs-derived catalysts are monometallic MOFs. The physicochemical properties of MOFs largely depend on the isolated metal centers or metal clusters in the MOFs matrix, and the involvement of multimetallic MOFs in the reaction is prone to instability, which limits the further application of MOFs.

In this work, Fe-doped ZIF-67 was combined with carbon fibers to enhance the catalytic activity of MOFs and the reusability during catalytic reactions. In addition, the 2-methylimidazole backbone was partially replaced using 5,6-dimethylbenzimidazole to further improve the water stability. The ordered Fe, Co bimetallic ZIF(Fe/Co)$_x$@CNF materials were successfully synthesized by a simple method. To evaluate the catalytic performance of the materials, ceftiofur sodium was degraded by activating PMS in aqueous solution with different conditions (pH, PMS dose, and catalyst). The results showed that ZIF(Fe/Co)$_x$@CNF exhibited excellent PMS activation performance, achieving 93.2% CEF (25 ppm) removal in 20 min. In addition, we prepared ZIF(Fe/Co)$_x$@CNF with different molar ratios (Fe/Co) for comparative experiments of CEF degradation. The mechanism of the synergistic response of bimetallic ZIF(Fe/Co)$_x$@CNF to PMS activation was investigated in detail based on the results of X-ray photoelectron spectroscopy and comparative experiments.

2. Experiments

2.1. Chemical Substances. The chemical substances and reagents used in the experiments included cobalt nitrate hexahydrate ($Co(NO)_3{\bullet}6H_2O$, ≥98.5%), ferric trichloride

hexahydrate ($FeCl_3 \bullet 6H_2O$, ≥98.5%), 2-methylimidazole ($C_4H_6N_2$, 98.0%) purchased from Aladdin Industrial Co. Ltd. (Shanghai, China). 5,6-dimethylbenzimidazole ($C_9H_{10}N_2$, ≥99.72%), triethylamine ($C_6H_{15}N$, AR, ≥99%), sodium hydroxide (NaOH, AR, ≥99%), acetone (C_3H_6O, AR, ≥99%) purchased from Sinopharm Chemical Reagent Co. Ltd, Wos1009 carbon fiber cloth purchased from Taiwan Carbon Energy Co. Ltd. All the above chemical reagents were not further purified.

2.2. Pretreatment with Carbon Fiber. Wos1009 carbon cloth was used, and carbon nanofiber was prepared from the carbon cloth, pretreated with 200 ml acetone, refluxed in an oil bath at 70°C for 48 h. After the completion of the oil bath, it was washed 3 times with ethanol and water, and dried overnight at 60°C under vacuum.

2.3. Preparation of Fe/Co-ZIF@CNF by Solvothermal Method. 0.2 g NaOH and 1.38 g 2-methylimidazole were dissolved in 10 ml water and configured as solution A. The carbon nanofiber was uniformly distributed in the solution by ultrasonication and stirred for 3 h. 0.116 g $Co(NO_3)_2 \bullet 6H_2O$ and 0.108 g $FeCl_3 \bullet 6H_2O$ were dissolved in 6 ml of water to configure solution B. The B solution was slowly added dropwise to the A solution under ultrasonication, stirred for 3 h, and washed with ethanol three times, and the resulting purple fiber product was dried in an oven at 60°C under vacuum overnight.

2.4. Synthesis of DMBIM-Modified ZIF(Fe/Co)$_x$@CNF. The synthesis of ZIF(Fe/Co)$_x$@CNF is shown in Figure 1. The prepared Fe/Co-ZIF@CNF was placed in methanol solution in the ratio of 1 : 80 to form solution C. DMBIM was dissolved in the same amount of methanol (Meth), and TEA was added to form solution D, keeping Fe/Co-ZIF@CNF : DMBIM : TEA : Meth as 1 : 1 : 1 : 160. Solution C was then mixed with Solution D and heat-treated in an oil bath at 60°C for 24 h. The resulting purple fiber products were dried in an oven at 60°C under vacuum overnight.

2.5. Characterization Methods. The crystalline phases of ZIF-67, CNF, Fe/Co-ZIF, Fe/Co-ZIF@CNF, and ZIF(Fe/Co)$_x$@CNF were determined by X-ray diffraction (XRD, Bruker D8, GER) with 2θ in the range of 5–60°. The infrared spectra of ZIF(Fe/Co)$_x$@CNF were determined by Fourier infrared spectrometer (FT-IR, Nicolet iS5, USA) and compared with pure ZIF-67, CNF, and DMBIM to determine the surface functional groups and the chemical structure changes between them. The nitrogen adsorption-desorption isotherms of ZIF(Fe/Co)$_x$@CNF were recorded by a gas sorption analyzer (BET, ASAP 2460, USA), and the specific surface area was estimated by Barrett–Emmett–Teller (BET) theory. Meanwhile, the chemical states of the newly prepared and reacted ZIF(Fe/Co)$_x$@CNF were determined by X-ray photoelectron spectroscopy (XPS, Escalab, 250Xi, USA), respectively. The surface morphology and structure of ZIF(Fe/Co)$_x$@CNF and Fe/Co-ZIF were observed by scanning electron microscopy (SEM, FEI Quanta FEG, USA). Chromatographic separation was established using an Eclipse C18 column (3.0 mm × 150 mm × 3.5 μm) and high-performance liquid chromatography (HPLC, UltiMateTM3000, JPN) with a mobile phase consisting of acetonitrile/water (60 : 40, v/v) mixture at a flow rate of 0.8 mL/min. The concentration of CEF in the solution was detected at different times with a detector wavelength of 292 nm. In addition, to evaluate the mineralization rate of the MOFs/PMS system, the residual organic carbon content in the reaction solution was measured by a total organic carbon analyzer (TOC, Elementer Vario-TOC Cobe, GER). The electrochemical measurements were all carried out at the electrochemical station (CHI 660D, CHN).

2.6. Catalytic Performance Evaluation. The degradation of CEF was carried out at room temperature in a 250 mL glass beaker by homogeneous stirring. Generally, the experimental solution is composed of a mixture of 100 mL of CEF solution (25 mg/L) and 10 mg of ZIF(Fe/Co)$_x$@CNF catalyst. Since the DMBIM-modified material has a smaller contact angle with water, that is, it is more hydrophobic, the reaction was started by adding 30 mg PMS after 30 min of stirring. In the reaction, an amount of NaOH (0.1 mM) was added to adjust the initial pH of the experimental solution to neutral. During the reaction, 1 mL of solution sample was taken from the experimental solution at regular intervals and filtered using a 0.22 μm nylon membrane filter head to remove the catalyst, and then, 1 mL of Meth was injected into the solution sample to quench the free radical reaction. The concentration of CEF in the solution was measured by HPLC, and all experiments were performed at least twice to verify the reproducibility of the results, with detailed measurement parameters provided in the characterization.

3. Results and Discussion

3.1. Structure and Composition Characterization. As shown in Figure 2(a), XRD analysis of the obtained samples was performed. By comparison of the diffraction peaks, the doping of Fe^{3+} did not damage the crystal structure of ZIF-67, and the structural information of Fe/Co-ZIF was similar to that of ZIF-67. The two diffraction peaks near 26° and 43° represent CNF corresponding to the (002) and (100) crystallographic planes of carbon, respectively. Compared with ZIF-67, the diffraction peaks of Fe/Co-ZIF are shifted to a small angle, presumably because the lattice constant becomes larger due to the replacement of smaller Co^{2+} by larger Fe^{3+} ions on the ZIF-67 backbone [35]. Meanwhile, the formation of Fe/Co-ZIF was not affected by CNF. And after the reaction, the XRD pattern of the ZIF(Fe/Co)$_x$@CNF has no obvious change. The surface functional groups and the chemical structure changes between different catalysts were further measured by FT-IR spectroscopy. As shown in Figure 2(b), the main components of ZIF-67 are the cobalt ion center and the 2-methylimidazole ligand. Therefore, most of the characteristic bands of ZIF-67 are associated with the imidazole ring in 2-methylimidazole. The peak at

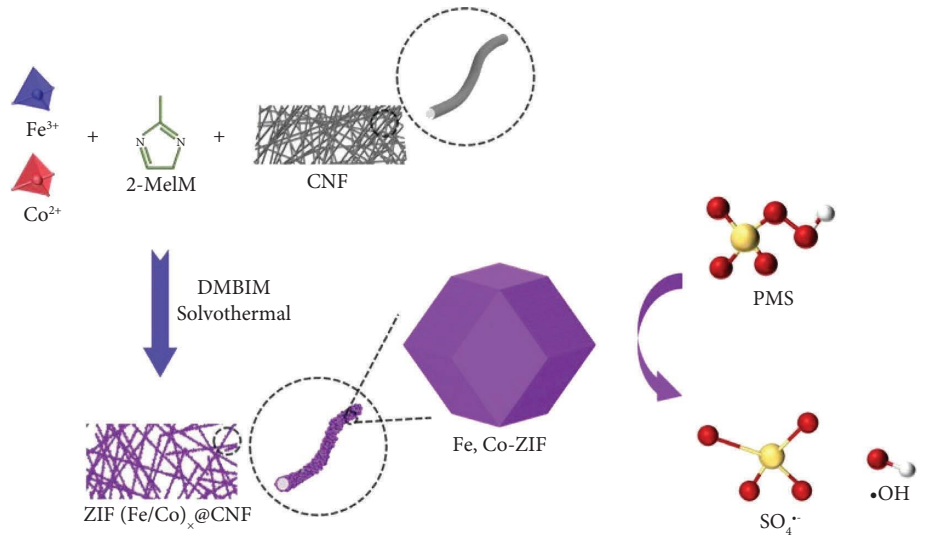

Figure 1: Schematic illustration of the synthesis of ZIF(Fe/Co)$_x$@CNF for CEF degradation.

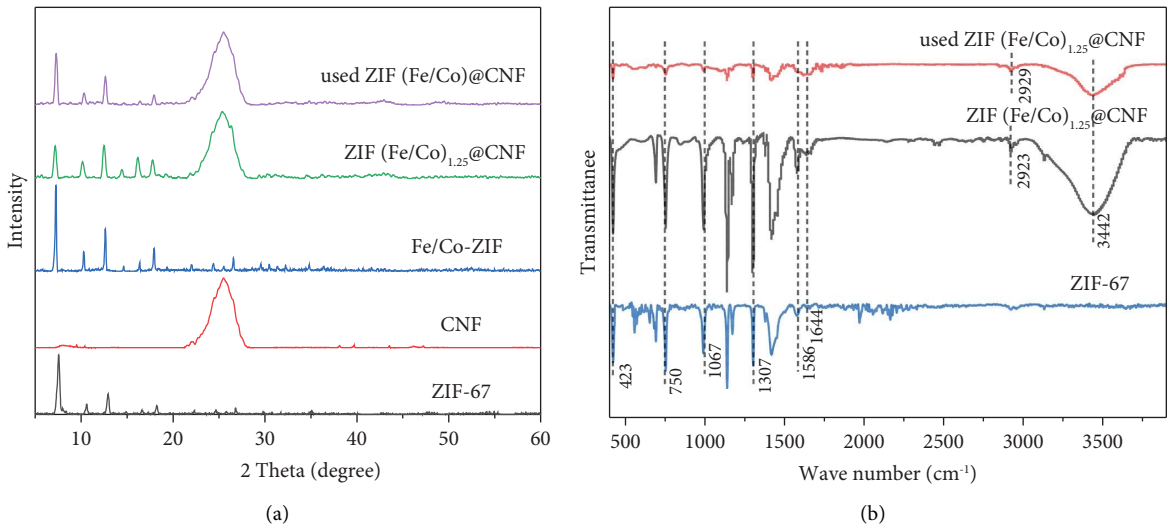

Figure 2: (a) XRD pattern of ZIF(Fe/Co)$_x$@CNF and (b) FTIR spectrum of ZIF(Fe/Co)$_x$@CNF.

423 cm^{-1} represented the Co-N stretching vibration, and the absorption peak at 1307 cm^{-1} was considered the C-N in ZIF-67, indicating the presence of ZIF-67 [36, 37]. The peak of the C-H bending vibration of the benzene ring occurred at 750 cm^{-1}, and the spectral band at 700–900 cm^{-1} was associated with the C-H bending vibration of CNF, overlapping with the band corresponding to the out-of-plane vibration of the imidazole ring [38]. The energy band near 1067 cm^{-1} was assigned to the stretching and deformation of the C-O-C stretching vibration. The absorption bands at 1586 cm^{-1} and 1644 cm^{-1} were assigned to C=N and C=O stretching vibrations [39]. And the spectral bands located at 3344 and 2899 cm^{-1} may be associated with OH and CH$_n$ stretching vibrations of CNF [40]. Meanwhile, the N-H stretching vibration band of DMBIM almost disappears between 2500-3150 cm^{-1}, providing strong evidence for the deprotonation coordination process of DMBIM [41].

The SEM images of Fe/Co-ZIF in Figures 3(a) and 3(b) revealed that the rhombic dodecahedral structure of Fe/Co-ZIF was similar to that of ZIF-67. Evidently, the ZIF(Fe/Co)$_x$@CNF exhibited a remarkably good inheritance of the polyhedral morphology of ZIF-67 crystals (Figures 3(c) and 3(d)). Studies have shown that the crystalline size of Fe/Co-ZIF materials increases significantly with an increase in Fe/Co ratio [35, 42]. The diameter of Fe/Co-ZIF$_{1.0}$ (1.0 refers to a Fe/Co ratio of 1.0) was about 1.5 μm, larger than that of ZIF-67 (about 0.4 μm). This may be due to the lattice distortion caused by the elongated ZIF-67 frame during the incorporation of Fe^{3+}. As a large metal ion, Fe^{3+} has a long coordination bond, which may promote the transformation of the material structure due to the reduction of steric hindrance effect [43, 44]. When Fe/Co-ZIF was combined with the CNF, the outer wall of CNF was uniformly covered by MOFs NPs, and the size of these Fe/Co-ZIF was much

smaller than that of the pure Fe/Co-ZIF crystals. The microstructure of CNFs may limit the growth of MOFs microcrystals, resulting in the decrease in size and affecting the distribution, which was in correlation with previous studies [45, 46].

In order to determine the gas adsorption capability of ZIF-67@CNF and ZIF(Fe/Co)$_x$@CNF, N_2 adsorption and desorption isotherms are measured as shown in Figure 4 and Table 1. Clearly, ZIF(Fe/Co)$_x$@CNF with dodecahedral morphology shows the largest BET surface area of 1350.073 $m^2 \cdot g^{-1}$ with a pore volume of 0.51 $cm^3 \cdot g^{-1}$. At low relative pressure, the isotherm rose rapidly, and the adsorption volume increased, indicating the presence of micropores in all samples. In addition, the green curve representing ZIF(Fe/Co)$_x$@CNF increases N_2 adsorption near $P/P_0 = 1$, indicating high intergranular porosity of ZIF(Fe/Co)$_x$@CNF. Meanwhile, the adsorption and desorption curves of the two samples showed no obvious hysteresis loops. It indicates that the adsorption and desorption process of the two materials is a complete process, and the residual adsorption capacity is close to the adsorption capacity of the same pressure, which means that the pore walls of the two materials are smooth, the pore opening is good, and the pore section diameter is uniform.

The XPS spectra of ZIF(Fe/Co)$_x$@CNF were investigated to further explore the composition and valence states of the elements on the composite surface. As shown in Figure 5(a), the ZIF(Fe/Co)$_x$@CNF sample consists of C, N, O, Fe, and Co elements [47–49]. The high-resolution XPS spectra of C 1s shown in Figure 5(b) can be fitted with three peaks located at 284.8, 286.0, and 288.5 eV. The main peak at 284.8 eV corresponds to the C-C as well as C=C bonds in the methylimidazole ring [49–52]. The peaks at 286.0 eV and 288.5 eV mainly correspond to C-N and C=N, which indicates that the nitrogen elements were successfully doped into the carbon framework. Moreover, the high-resolution spectrum of Fe 2p shows (Figure 5(c)) that multiple valence states of the element Fe coexist in ZIF(Fe/Co)$_x$@CNF. The high-resolution spectrum of Fe 2p was convolved with eight peaks that can be fitted to three components corresponding to Fe^{2+} (710.8 eV, 723.8 eV), Fe^{3+} (712.5 eV, 725.6 eV) and the corresponding satellite peaks (714.3 eV, 718.7 eV, 730.4 eV, and 733.8 eV), thus verifying that Fe^{2+} and Fe^{3+} are the main valence states of Fe in ZIF(Fe/Co)$_x$@CNF materials. The high-resolution spectrum of Co 2p is shown in Figure 5(d), and the two main peaks located at 781.0 eV and 796.6 eV can be attributed to Co 2p 3/2 and Co 2p 1/2, respectively. In addition, the satellite peaks corresponding to Co 2p 3/2 at 786.2 eV and Co 2p 1/2 at 802.7 eV are recorded, indicating that the Co ions in ZIF(Fe/Co)$_x$@CNF exist in the high-spin Co^{2+} state [53, 54].

3.2. Catalytic Properties. The catalytic performance of the prepared ZIF(Fe/Co)x@CNF for activation of PMS to degrade CEF was evaluated. As shown in Figure 6, the degradation of CEF by PMS alone was extremely slow, with only 8.9% of CEF degraded within 20 min. This suggested that PMS could hardly degrade CEF without catalysts. When only ZIF(Fe/Co)$_x$@CNF was added, only 1.1% of CEF was removed from the reaction system within 20 min, which was mainly attributed to the adsorption of CEF by ZIF(Fe/Co)$_x$@CNF. The CEF degradation efficiency was 6.2% when CNF and PMS reagents were simultaneously added, indicating that the CNF itself has a limited ability to activate PMS. In addition, the degradation rate of CEF by the Fe/Co-ZIF/PMS system was increased from 89.9% to 92.2% compared with the monometallic ZIF-67/PMS system, which confirmed that the doping of Fe facilitated the activation of PMS. The degradation rate of the ZIF(Fe/Co)$_x$@CNF/PMS system towards CEF was 93.4% at 20 min when the bimetallic Fe/Co-ZIF was prepared on CNF, and DMBIM was introduced to replace the 2-methylimidazole backbone to improve the material stability. The k_{obs} for CEF degradation in the ZIF-67/PMS system (0.134 min^{-1}), Fe/Co-ZIF/PMS system (0.145 min^{-1}), and ZIF(Fe/Co)$_x$@CNF/PMS system (0.151 min^{-1}) is shown in the illustration in Figure 6. This further confirmed the promoting role of Fe^{3+} as well as DMBIM incorporation in CEF degradation.

The effects of Fe/Co ratios on the CEF degradation are shown in Figure 7. The catalytic performance of ZIF(Fe/Co)$_x$@CNF was investigated through the oxidative degradation of CEF by activating PMS on ZIF(Fe/Co)$_x$@CNF. All experiments were performed after a 30 min homogeneous stirring, indicating that ZIF(Fe/Co)$_x$@CNF did not have a significant adsorption effect on CEF. The CEF removal efficiency reached 94.3% in ZIF(Fe/Co)$_x$@CNF/PMS system, and it increased gradually with the increase of Fe ratio in the composite. With the Fe/Co molar ratio reached to 1.25 : 1, the ZIF(Fe/Co)$_{1.25}$@CNF exhibited the highest catalytic activity with a degradation efficiency of 97.4%. However, the continuation of Fe^{3+} doping on this basis would cause different degrees of damage to the skeletal structure of ZIF-67, thus decreasing the degradation efficiency. Moreover, the addition of ZIF(Fe/Co)$_x$@CNF effectively improved the degradation rate of the reaction system. As shown in the illustration in Figure 7, the ZIF(Fe/Co)$_x$@CNF/PMS system reached the maximum k_{obs} when Fe doping ratios reached about 1.2 to 1.5, further determining the choice of the optimal Fe/Co mass ratio of the catalytic material.

The catalytic performance of the ZIF(Fe/Co)$_{1.25}$@CNF/PMS system was further investigated by studying the effect of different concentrations of ceftiofur sodium (CEF) on the catalytic performance. The degradation effect of ZIF(Fe/Co)$_{1.25}$@CNF with different concentrations of CEF is shown in Figure 8, and the apparent rate constant (k_{obs}) was used to reflect the CEF degradation rate (illustration in Figure 8). The ZIF(Fe/Co)$_{1.25}$@CNF showed satisfactory catalytic performance in different CEF concentration ranges. It is worth mentioning that CEF was almost completely degraded at the concentration from 10 ppm to 30 ppm with k_{obs} in the high level range of 0.155 min^{-1} to 0.129 min^{-1}. With the CEF concentration further increased to 40 ppm and 50 ppm, only 93.4% and 86.4% of CEF were degraded after 40 min with k_{obs} of 0.071 min^{-1} and 0.066 min^{-1}. Considering the concentration of CEF in real wastewater is generally lower than several mg/L, the ZIF(Fe/Co)$_x$@CNF/PMS system is likely to be applied to degrade CEF in practical wastewater treatment.

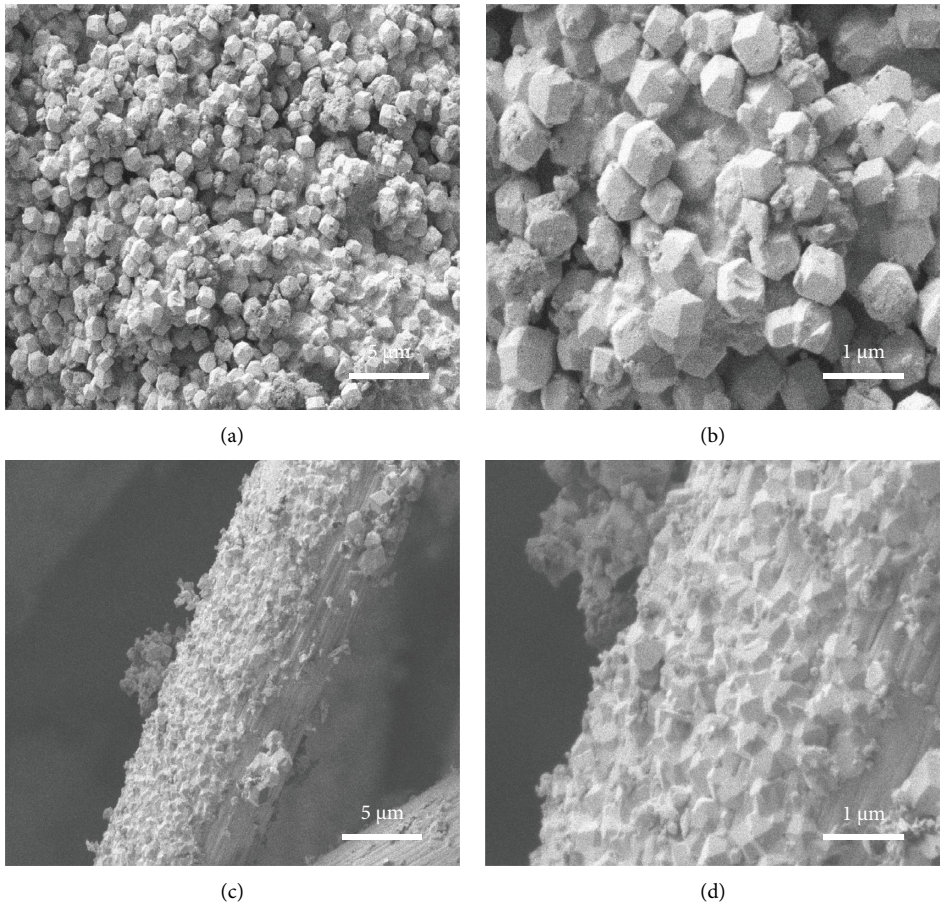

Figure 3: Scanning electron microscope (SEM) images of Fe/Co-ZIF (a, b) and ZIF(Fe/Co)$_x$@CNF (c, d).

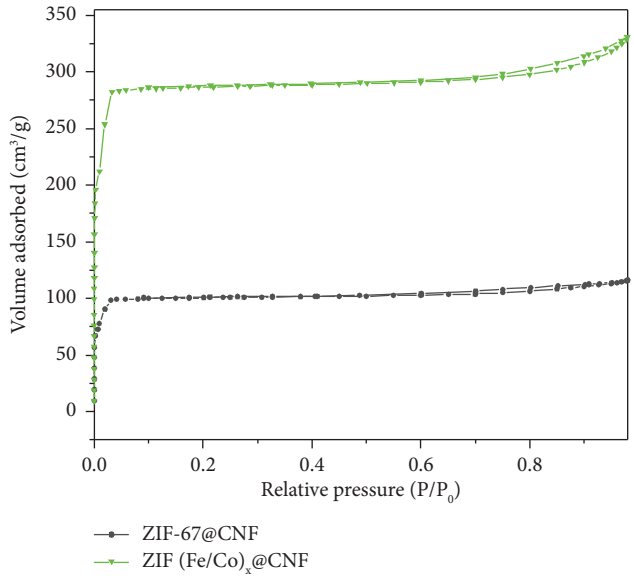

Figure 4: Nitrogen adsorption and desorption curves of ZIF-67@CNF and ZIF(Fe/Co)$_x$@CNF.

The effects of different PMS doses on the degradation of CEF are shown in Figure 9. When the dose of PMS was 0.1 g/L, only 64.7% of CEF was degraded in the reaction system with k_{obs} of 0.038 min^{-1}. This was mainly due to the lack of sufficient reactive radicals for the degradation of CEF. When the PMS dosage increased to 0.2 g/L, the degradation

Table 1: The specific surface area average pore size and pore volume of ZIF-67 and Fe/Co-ZIF.

Adsorbents	Surface area (m^2/g)	Average pore diameter (nm)	Pore volume (cm^3/g)
ZIF-67@CNF	455.743	1.5758	0.18
ZIF(Fe/Co)$_x$@CNF	1350.073	1.5182	0.51

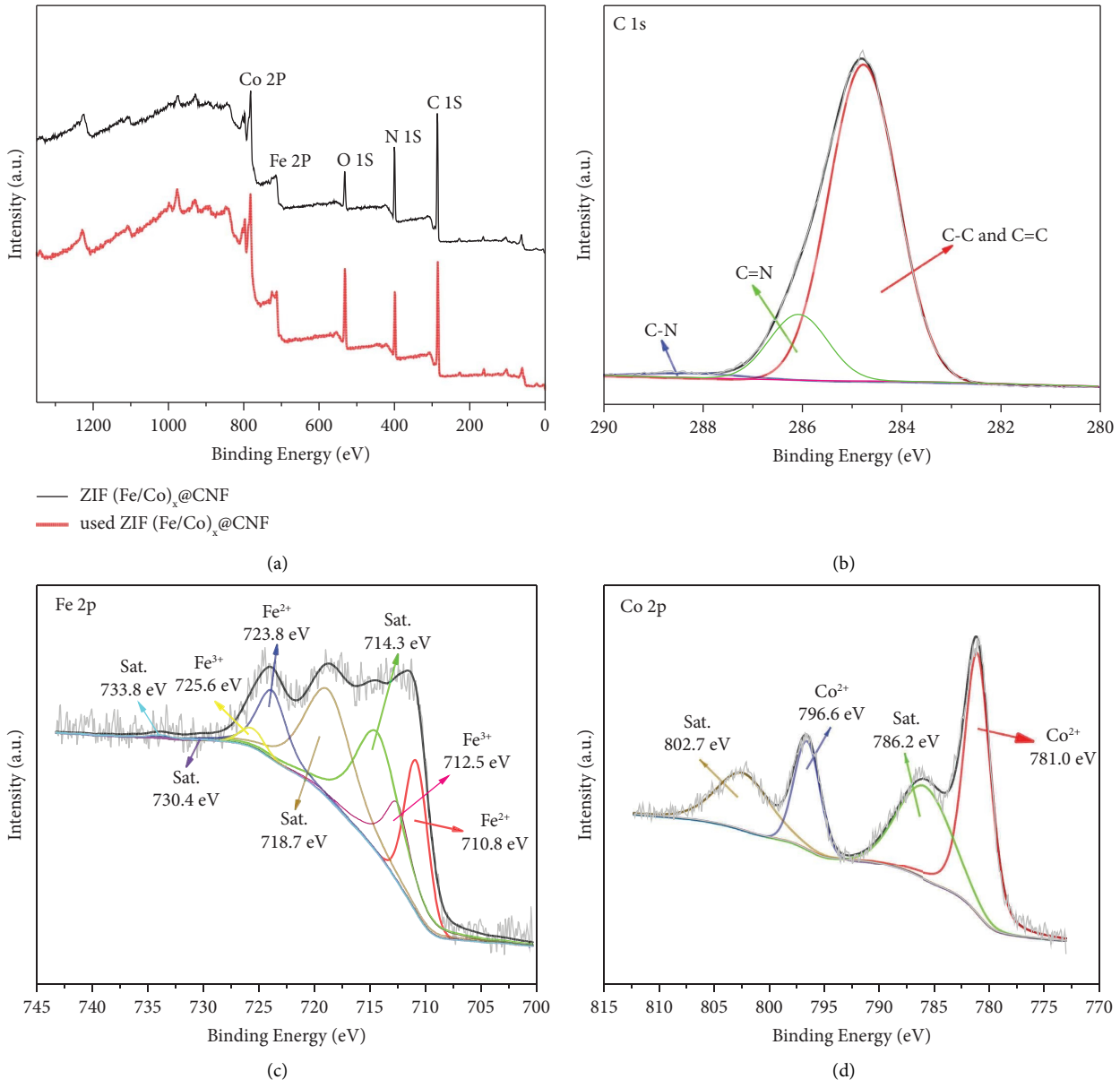

Figure 5: (a) XPS spectra of newly prepared ZIF(Fe/Co)$_x$@CNF; (b) XPS spectra of C 1s; (c) XPS spectra of Fe 2p; (d) XPS spectra of Co 2p.

efficiency and k_{obs} of CEF increased significantly to 91.2% and 0.108 min^{-1}. This suggested that at higher dosages, ZIF(Fe/Co)$_{1.25}$@CNF could activate PMS to produce more reactive species. The degradation efficiency of CEF reached to 97.4% and 92.6% with a further increase of PMS dosage from 0.3 to 0.4 g/L, and the corresponding k_{obs} are 0.152 min^{-1} and 0.132 min^{-1}, respectively. It was observed that the degradation rate of CEF was not significantly enhanced when the PMS dosage was increased to 0.3 g/L. According to the available studies, this may be due to the limited number of catalytic active sites of the material [42]. When the PMS dosage was further increased to more than 0.5 g/L, the corresponding CEF degradation rate and k_{obs} of the reaction at 20 min were significantly decreased to 70.6%

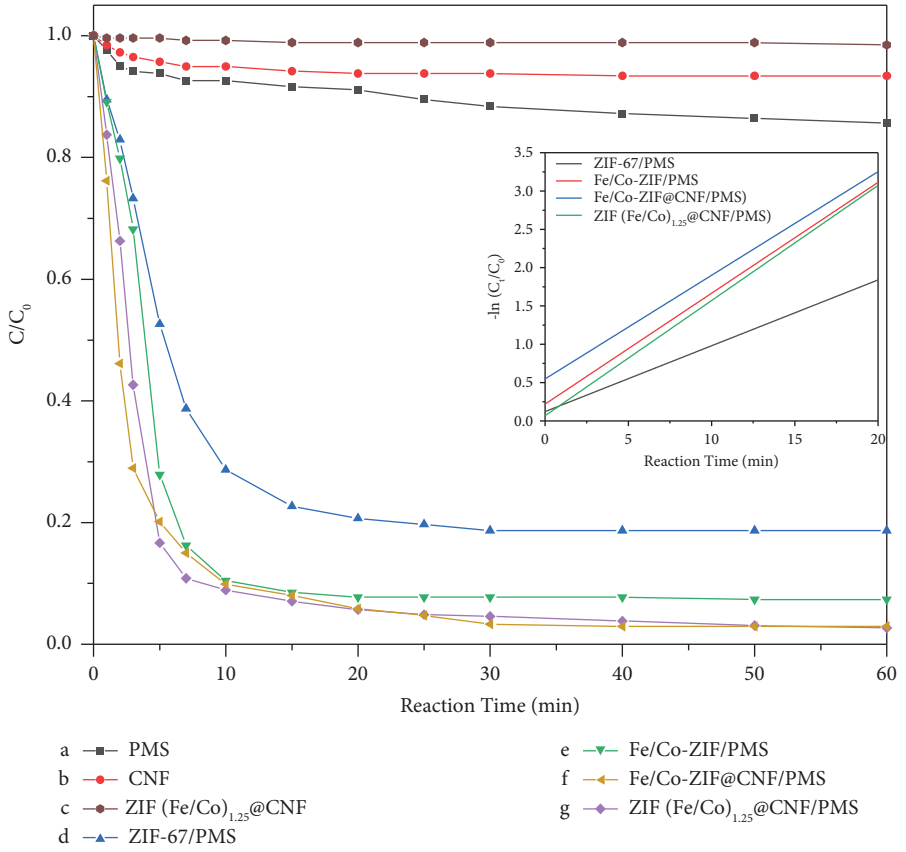

Figure 6: Degradation efficiency and kinetic performance of CEF in different systems. Conditions: [PMS] = 0.3 g/L, [catalyst] = 0.1 g/L, [CEF] = 25 mg/L, pH = 7.0, and temperature of 25°C.

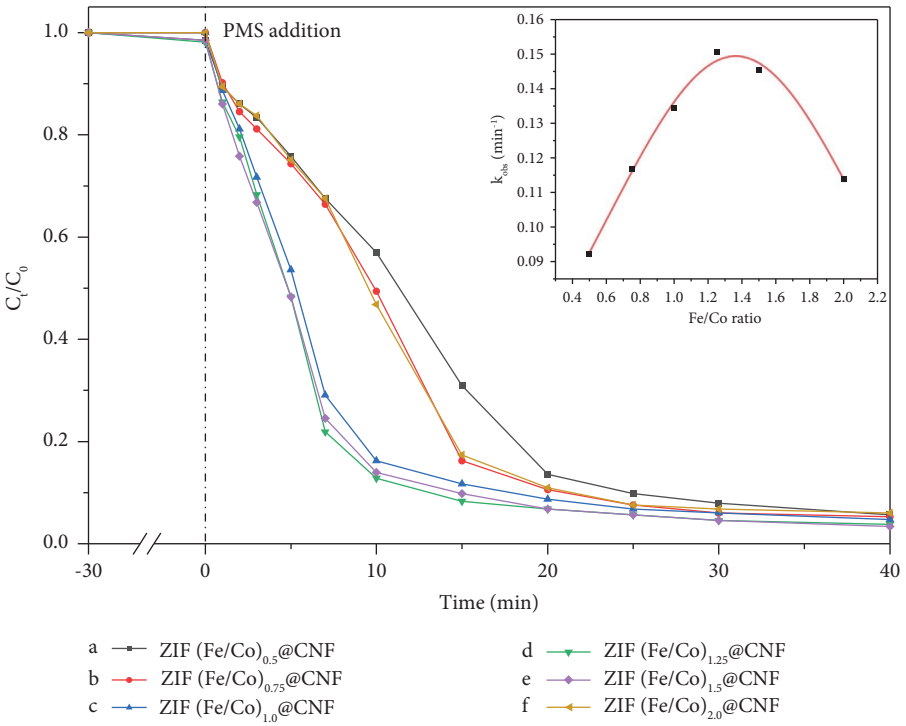

Figure 7: Effect of different Fe/Co mass ratios on CEF degradation. Conditions: [PMS] = 0.3 g/L, [catalyst] = 0.1 g/L, [CEF] = 25 mg/L, pH = 7.0, and temperature of 25°C.

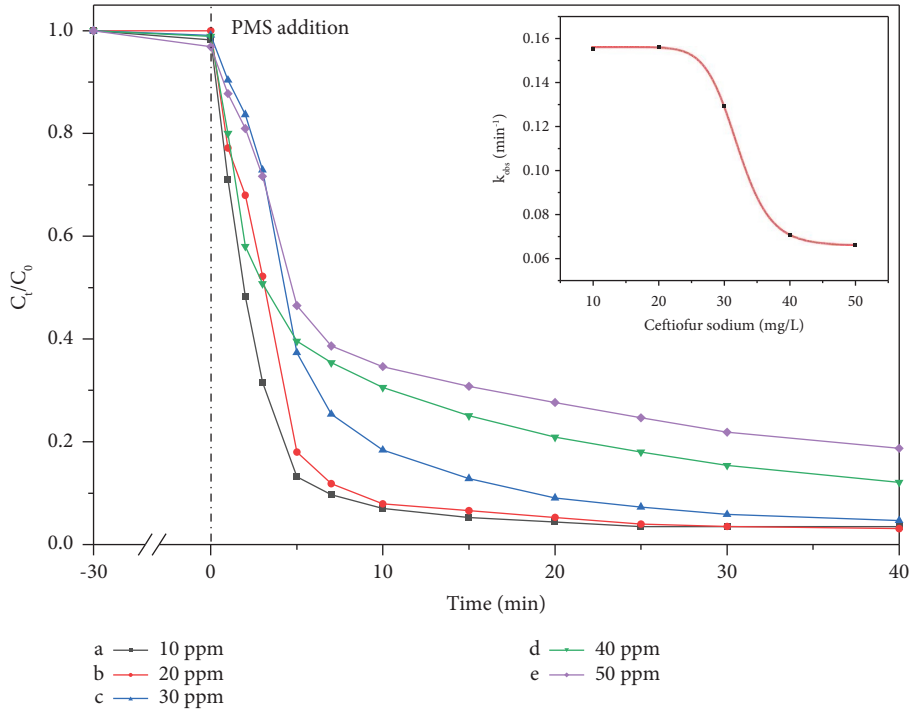

Figure 8: Effect of different CEF dosage on the degradation rate of CEF.

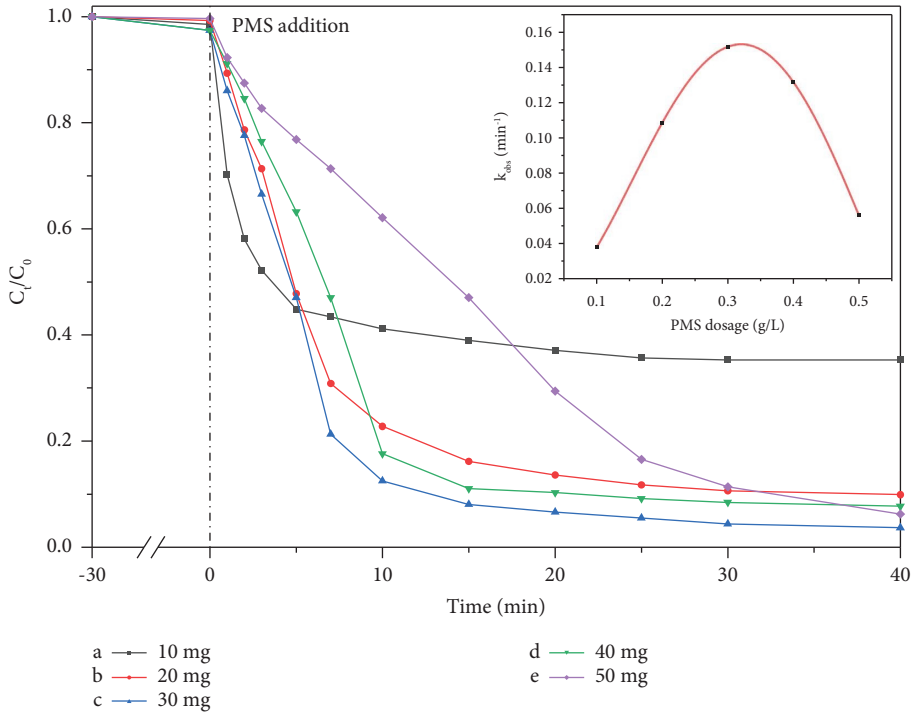

Figure 9: Effect of different PMS dosage on the degradation rate of CEF.

and 0.056 min^{-1}, respectively. This could be due to the self-quenching reaction of PMS adversely affecting the degradation of CEF (equations (1) and (2)) [55].

$$SO_4^{\bullet-} + SO_4^{\bullet-} \longrightarrow S_2O_8^{2-}, k = 4 \times 10^8\ M^{-1}S^{-1} \quad (1)$$

$$SO_4^{\bullet-} + {\bullet}OH \longrightarrow HSO_5^{-} \quad (2)$$

The catalytic performance of ZIF(Fe/Co)$_x$@CNF at different initial pH values was further investigated. It could be observed from Figure 10 that the degradation efficiency of CEF remained around 95% for the pH values of the reaction system between 5 and 9. The highest degradation efficiency of 97.4% was achieved when the pH value was between 7 and 8, while the degradation of CEF was only 65.44% at the extreme condition of pH 3. This may be caused by the binding of H^+ to the peroxide bond (O-O) of the PMS molecule. In addition, interfacial repulsion can lead to a weakening of the catalytic performance of the reaction system [56]. Meanwhile, the excess H^+ could react with •OH and $SO_4^{\bullet-}$ (equations (3) and (4)) [57–59]. In addition, since ZIF-67 is an acid-unstable structure, ZIF-67 in ZIF(Fe/Co)$_x$@CNF dissolves and releases Co^{2+} into the reaction solution under acidic conditions (5) [22, 60]. This limited the production of $SO_4^{\bullet-}$, leading to low elimination of CEF under acidic conditions. At the extreme condition of pH 11, the degradation efficiency of CEF reached 63.2%. This was probably due to the conversion of $SO_4^{\bullet-}$ to •OH (6), leading to a shift from an $SO_4^{\bullet-}$ dominated oxidation process to an •OH dominated oxidation process [61, 62]. In addition, the abundance of OH^- in the system under strongly alkaline conditions leads to the formation of cobalt hydroxide and iron hydroxide, which affects the efficiency of the reaction system. Furthermore, under strongly alkaline conditions, PMS exists mainly in the double anion form (SO_5^{2-}) instead of the single anion form (HSO_5^-). This might lead to the auto-decay of PMS and the associated production of $^1O_2$, making the degradation of CEF less efficient under extreme alkaline conditions [63, 64].

$$\bullet OH + H^+ + e^- \longrightarrow H_2O \quad (3)$$

$$SO_4^{\bullet-} + H^+ + e^- \longrightarrow HSO_4^{\bullet-} \quad (4)$$

$$Co^{2+} + H_2O \longrightarrow CoOH^+ + H^+ \quad (5)$$

$$SO_4^{\bullet-} + \bullet OH \longrightarrow \bullet OH + SO_4^{2-}, k = 4.6^- 8.3\times 107\ M^{-1}S^{-1} \quad (6)$$

Inorganic anions such as NO_3^-, HCO_3^-, Cl^-, and $H_2PO_4^-$ are ubiquitous in practical wastewater and can affect the efficiency of AOPs in several ways. To evaluate the effect of different inorganic anions on the removal efficiency of CEF, 1 mM and 2 mM of common anions (NO_3^-, HCO_3^-, Cl^-, $H_2PO_4^-$) were added to the ZIF(Fe/Co)$_x$@CNF/PMS system.

Based on previous studies, bicarbonate usually exhibits significant inhibition in metal-based catalytic/PMS systems [65]. As shown in Figure 11(a), in the ZIF(Fe/Co)$_x$@CNF/PMS system, the dose of HCO_3^- ranged from 1 mM to 2 mM, and the degradation rate of CEF decreased from 20.0% to 15.8%. This was mainly attributed to the fact that HCO_3^- acts as a quenching agent for $SO_4^{\bullet-}$ and •OH, reducing the concentration of reactive radicals in the reaction system (equations (7) and (8)) [66]. In addition, the addition of HCO_3^- caused a change in the pH of the solution, which reduces the efficiency of CEF removal [67].

$$SO_4^{\bullet-} + HCO_3^- \longrightarrow SO_4^{2-} + H^+ + CO_3^{\bullet-}, k = 9.1\times 10^6\ M^{-1}S^{-1} \quad (7)$$

$$\bullet OH + HCO_3^- \longrightarrow CO_3^{\bullet-} + H_2O, k = 8.5\times 10^6\ M^{-1}S^{-1} \quad (8)$$

It has been reported that Cl^- is easily reacted with radicals to form weaker radicals [68]. In contrast, the removal efficiency of CEF in the ZIF(Fe/Co)$_x$@CNF/PMS system decreased to 88.7% and 84.5% after the addition of 1 mM and 2 mM Cl^-, respectively (Figure 11(b)). In general, the degradation efficiency of pollutants would decrease with the addition of Cl^-. This inhibition may be due to the fact that Cl^- can act as a probe to consume $SO_4^{\bullet-}$ (9) and •OH (10) to produce chloride radical anions with lower redox potential. More importantly, the added Cl^- also directly consumes the oxidant PMS (equations (11) and (12)), which reduces the removal efficiency of CEF. Meanwhile, it has been reported that the direct reaction between Cl^- and PMS to form HOCl can improve the CEF removal efficiency to some extent (equations (11)–(13)) [69, 70]. Therefore, the inhibitory effect of Cl^- on CEF removal efficiency is not as pronounced as that of HCO_3^-.

$$SO_4^{\bullet-} + Cl^- \Longleftrightarrow SO_4^{2-} + \bullet Cl, k_f = 4.7\times 10^8\ M^{-1}S^{-1};\ k_r = 2.5\times 10^8\ M^{-1}S^{-1} \quad (9)$$

$$\bullet OH + Cl^- \Longleftrightarrow \bullet HOCl^-, k_f = 4.3\times 10^9\ M^{-1}S^{-1};\ k_r = 6.1\times 10^9\ M^{-1}S^{-1} \quad (10)$$

$$HSO_5^- + Cl^- \Longleftrightarrow SO_4^{2-} + HOCl \quad (11)$$

$$HSO_5^- + 2Cl^- + H^+ \longrightarrow SO_4^{2-} + Cl_2 + H_2O \quad (12)$$

$$Cl_2 + H_2O \longrightarrow HOCl + H^+ + Cl^- \quad (13)$$

NO_3^- not only can partially eliminate ROS but also consumes some PMS by direct reaction with PMS [71]. As shown in Figure 11(c), the degradation of CEF decreased to 87.2% and 84.6% in the presence of 1 mM and 2 mM NO_3^-, respectively. This was consistent with the results of previous studies [72]. In addition, this phenomenon may be due to the

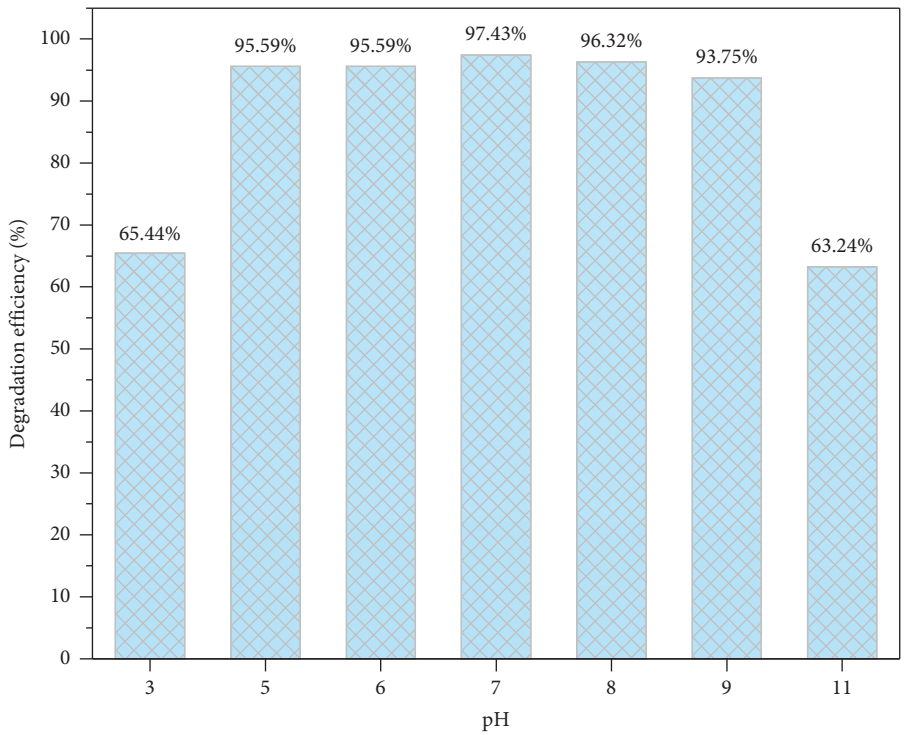

Figure 10: Effect of different pH on the degradation rate of CEF.

complexation between the catalyst and NO_3^- that inhibits the activation of PMS on the surface [73]. Meanwhile, the CEF removal rate also decreased to 85.7% and 91.7% after the addition of 1 mM and 2 mM $H_2PO_4^-$, respectively (Figure 11(d)). This suggests that $H_2PO_4^-$ forms phosphate with low oxidative activity by eliminating $SO_4^{\bullet-}$ and •OH [74]. Moreover, $H_2PO_4^-$ can chelate with cobalt ions on the catalyst surface to form complexes. This could hinder the binding of surface active sites to PMS, thus inhibiting the removal of CEF [75]. Nevertheless, $H_2PO_4^-$ can activate the PMS to improve the degradation of pollutants [76]. Therefore, the degradation efficiency of the reaction system for CEF was instead slightly improved after increasing the $H_2PO_4^-$ concentration from 1 mM to 2 mM. Compared to HCO_3^-, other anions including NO_3^- and $H_2PO_4^-$ plasma have very limited quenching potential for reactive radicals (equations (14)–(16)); thus, they have a relatively minor effect on CEF degradation [67, 77].

$$SO_4^{\bullet-} + NO_3^- \longrightarrow SO_4^{2-} + \bullet NO_3, k = 5.5 \times 10^5\ M^{-1}S^{-1} \quad (14)$$

$$SO_4^{\bullet-} + H_2PO_4^- \longrightarrow SO_4^{2-} + \bullet H_2PO_4^-, k < 7 \times 10^4\ M^{-1}S^{-1} \quad (15)$$

$$\bullet OH + H_2PO_4^- \longrightarrow OH^- + \bullet H_2PO_4^-, k = 2 \times 10^4\ M^{-1}S^{-1} \quad (16)$$

As shown in Figure 12, humic acid (HA) is one of the most common natural organic compounds in water. Therefore, different amounts of HA were added to the ZIF(Fe/Co)$_x$@CNF/PMS system to evaluate the effect of macromolecular organic compounds on the CEF removal efficiency. Clearly, the CEF removal rate was significantly reduced to 89.9% after the addition of 10 ppm HA and further reduced to 86.8% with the increase of HA concentration. This phenomenon can be explained by the partial shielding of the surface active site on ZIF(Fe/Co)$_x$@CNF/PMS by HA, which is consistent with previous studies [78].

3.3. Mechanism of ROS Identification and Degradation. To verify the specific ROS generated during CEF degradation, relevant quenching experiments were performed. In existing studies, $SO_4^{\bullet-}$ and •OH are the main ROS during PMS activation with metal-based catalysts. Therefore, Meth, TBA, and FFA were used to quench the ROS involved in the ZIF(Fe/Co)$_x$@CNF/PMS system. As shown in Figure 13(a), at the addition of 1000 mM Meth, the degradation rate of CEF was determined to be 37.4%. When 1000 mM TBA was added, the degradation rate of CEF remained at a high level of 90.7% after 20 min, which was only slightly decreased compared with 93.2% when no quenching agent was added. This is probably due to the fact that methanol can be used as a scavenger for both $SO_4^{\bullet-}$ ($k = 3.2 \times 106\ M^{-1}s^{-1}$) and •OH ($k = 9.7 \times 108\ M^{-1}s^{-1}$), while TBA can only quench •OH ($k = 3.2 \times 108\ M^{-1}s^{-1}$). These results indicated that both $SO_4^{\bullet-}$ and •OH affected the degradation of CEF, and the contribution of $SO_4^{\bullet-}$ was much larger than that of •OH. To further identify the reactive radicals in the ZIF(Fe/Co)$_x$@CNF/PMS system, EPR experiments were carried out using DMPO as a spin trapping agent. As shown in Figure 13(b), PMS cannot generate reactive radicals by itself in the absence

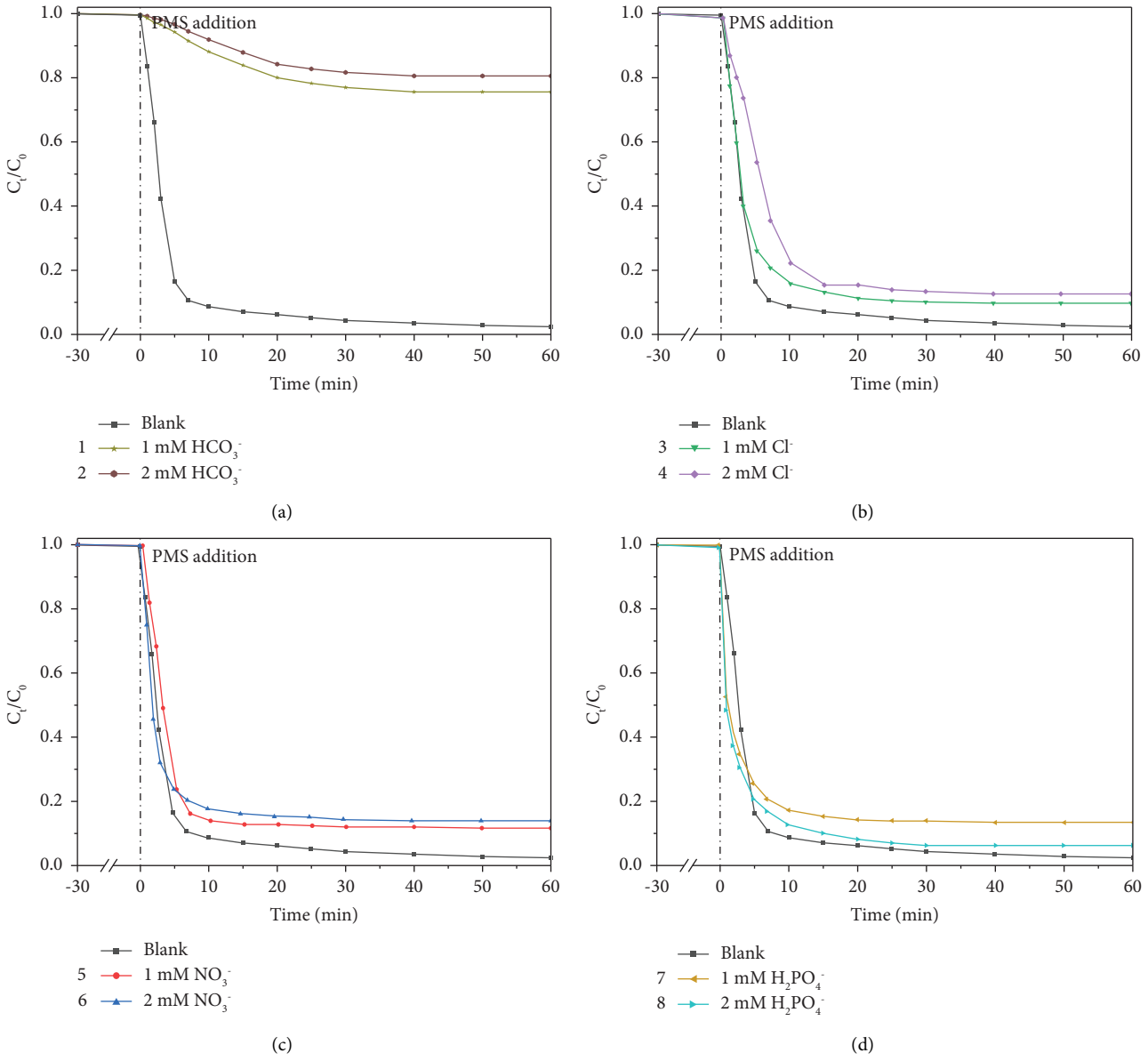

Figure 11: Effect of inorganic anions on CEF degradation. Conditions: [PMS] = 0.3 g/L, [catalyst] = 0.1 g/L, [CEF] = 25 mg/L, pH = 7.0, and temperature of 25°C.

of the catalyst. After the addition of catalysts, the characteristic peaks of DMPO-$SO_4^{\bullet\mp}$ and DMPO-•OH were still uncaptured, but distinctive characteristic peaks corresponding to DMPOX (5,5-dimethyl-2-oxo-pyrroline-1-oxyl) appeared (1 : 2:1 : 2 : 1 : 2 : 1) [79, 80]. This does not imply the absence of $SO_4^{\bullet-}$ and •OH during the reaction, which represents that DMPO is more susceptible to be oxidized by strong oxidants such as $SO_4^{\bullet-}$ and •OH in this system, rather than capturing these radicals. Nevertheless, the variation in the number of free radicals during the reaction can still be reflected by comparing the peak intensity of DMPOX. The peak of DMPOX could be clearly observed at 1 min, followed by a large peak value appearing at 5 min, representing the continuous generation of free radicals. These results suggested that both $SO_4^{\bullet-}$ and •OH were formed by catalyst activation of PMS decomposition, with $SO_4^{\bullet-}$ contributing more to the degradation of CEF.

$^1O_2$ is also considered an important ROS formed by PMS activation as shown in many studies, and thus, furfuryl alcohol (FFA) was used as a quenching agent to capture $^1O_2$. As shown in Figure 13(a), FFA had essentially no effect on the degradation of CEF, with the degradation rate changing from 97.4% to 95.4% after the addition of 1000 mM FFA. TEMP was used as a spin trapping agent for further EPR experiments. As shown in Figure 13(b), the EPR test detected a weak characteristic peak of TEMP-$^1O_2$ (1 : 1 : 1) at 5 min, indicating that only a small amount of $^1O_2$ generated in the ZIF(Fe/Co)$_x$@CNF/PMS system. This might be attributed to the slow autolytic production of $^1O_2$ by PMS (equation (17)). In summary, $^1O_2$ and •OH did not have

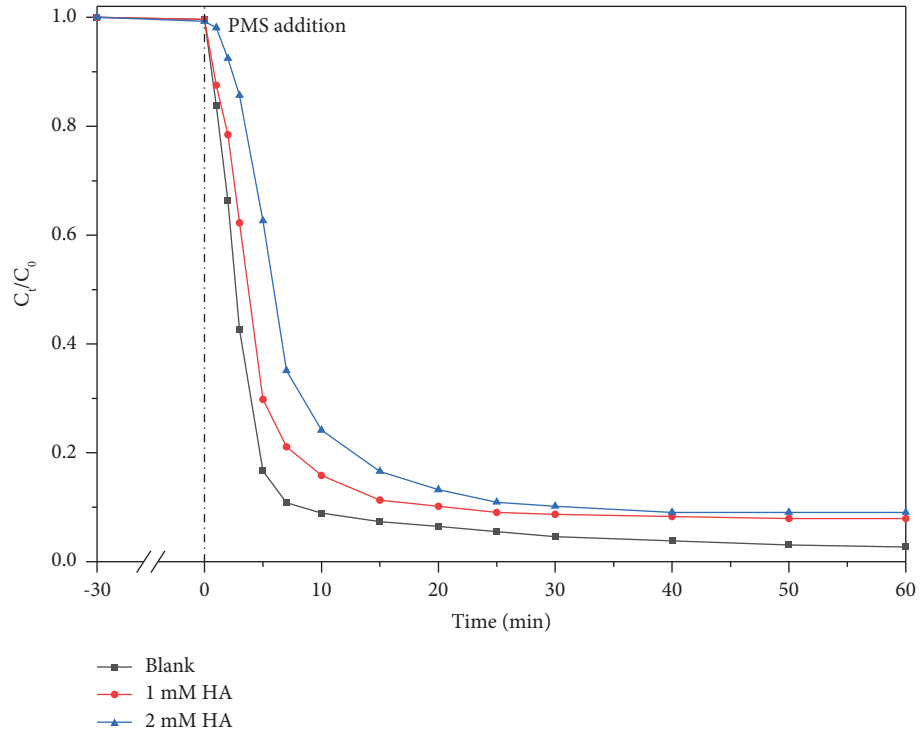

Figure 12: Effect of HA on CEF degradation. Conditions: [PMS] = 0.3 g/L, [catalyst] = 0.1 g/L, [CEF] = 25 mg/L, pH = 7.0, and temperature of 25°C.

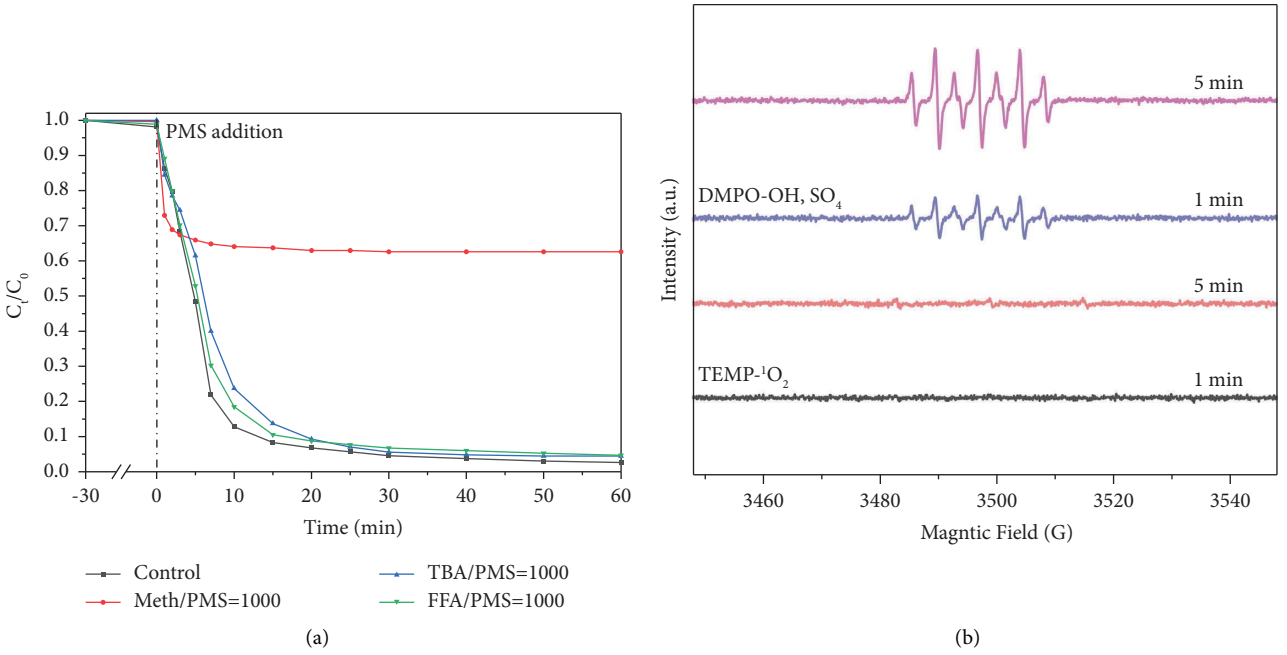

Figure 13: (a) Effect of different scavengers on the degradation efficiency of CEF in the ZIF(Fe/Co)$_x$@CNF/PMS system; (b) EPR spectra of ZIF(Fe/Co)$_x$@CNF activated PMS with TEMP and DMPO as trapping agents.

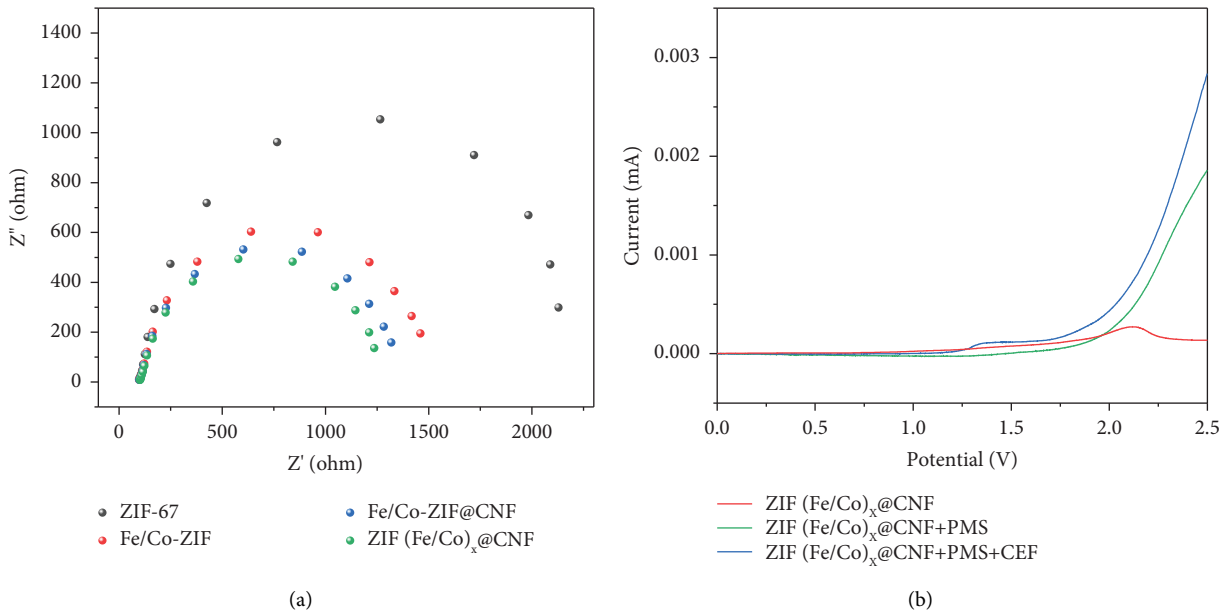

Figure 14: (a) EIS measurement of different catalysts (KOH = 0.1 mM); (b) linear-sweep voltammograms under different conditions at a scan rate of 5 mVs^{-1}.

a major effect on the degradation of CEF, while $SO_4^{\bullet\mp}$ was the main active substance in the reaction system.

$$HSO_5^- + SO_5^{2-} \longrightarrow HSO_4^- + SO_4^{2-} + {}^1O_2 \quad (17)$$

Electrochemical measurements were conducted to expound the electron transfer process during the degradation of CEF by ZIF(Fe/Co)$_x$@CNF/PMS system. Firstly, the electrochemical impedance spectroscopy (EIS) of different materials was measured to compare the electron transfer capacity of different catalysts. As shown in Figure 14(a), the Nyquist plot of ZIF(Fe/Co)$_x$@CNF composite observed a smaller semicircle diameter than that of ZIF-67, Fe/Co-ZIF, and Fe/Co-ZIF@CNF materials. This indicates that ZIF(Fe/Co)$_x$@CNF composite has the lowest charge transfer resistance and the fastest charge transfer rate compared with other materials. In addition, linear sweep voltammetry (LSV) was performed to evaluate the electrochemical properties of the ZIF(Fe/Co)$_x$@CNF composite surface, as shown in Figure 14(b). After the addition of 0.1 mM PMS, a significant increase in current density was observed in the LSV diagram, indicating an interaction between ZIF(Fe/Co)$_x$@CNF and PMS. The current density was then observed to increase again after the addition of CEF, indicating that the close interaction between ZIF(Fe/Co)$_x$@CNF, PMS, and CEF is essential for accelerating electron transfer from CEF to PMS and that the ZIF(Fe/Co)$_x$@CNF composite has excellent electrochemical properties.

The chemical valence changes of Fe and Co elements in ZIF(Fe/Co)$_x$@CNF before and after the degradation of CEF were analyzed by XPS. As shown in the high-resolution spectrum of Fe 2p in Figure 15(a), there was a significant change in the ratio of Fe^{2+}/Fe^{3+} before and after the reaction. Fe 2p 3/2 could be fitted with three peaks out of 710.6 eV, 712.5 eV, and 714.5 eV, corresponding to Fe^{2+}, Fe^{3+}, and the corresponding satellite peaks, respectively. In the fresh ZIF(Fe/Co)$_x$@CNF, the ratio of Fe^{2+}/Fe^{3+} was 1.78, while it decreased to 1.32 after the oxidation reaction. This suggests that Fe^{2+} is involved in the reaction of PMS, and there may be a synergistic effect between Fe^{2+} and Co^{3+}, which is thermodynamically favorable (equations (18) and (19)) [80, 81]. Similar to many previous reports, Fe^{2+} synergistic unsaturated metal sites can accelerate the autolytic generation of ROS from PMS, thus improving the catalytic performance (equations (20)–(22)) [82]. The high-resolution spectrum of Co 2p 3/2 (Figure 15(b)) could be fitted to two peaks at 780.5 eV and 781.6 eV, which were distinguished from that before the degradation reaction. This indicated the presence of Co^{2+} and Co^{3+} on the surface of ZIF(Fe/Co)$_x$@CNF after the reaction. After the CEF degradation, Co^{2+} in the ZIF-67 matrix was consumed to activate the autolytic decomposition of PMS and converted to Co^{3+} (23). However, the accumulation of strongly electron-absorbing Co^{3+} inhibits the aforementioned radical process reaction, which leads to a decrease in ROS production and catalytic activity [83]. The generated Co^{3+} is usually considered reconverted to Co^{2+} by trapping electrons (24). However, unlike the pathway generally considered, the large presence of Fe^{2+} in the ZIF(Fe/Co)$_x$@CNF could provide a convenient pathway for the capture of electrons and rapid reconversion of Co^{3+} to Co^{2+}. This mainly due to the fact that the standard redox potential of Co^{3+}/Co^{2+} (1.808 V) is much higher than the standard redox potential of Fe^{3+}/Fe^{2+} (0.771 V), as shown in equations (18) and (19). Therefore, the generated Co^{3+} is reconverted to Co^{2+} by capturing electrons from Fe^{2+}, while Fe^{2+} is converted to Fe^{3+} (equation (25)).

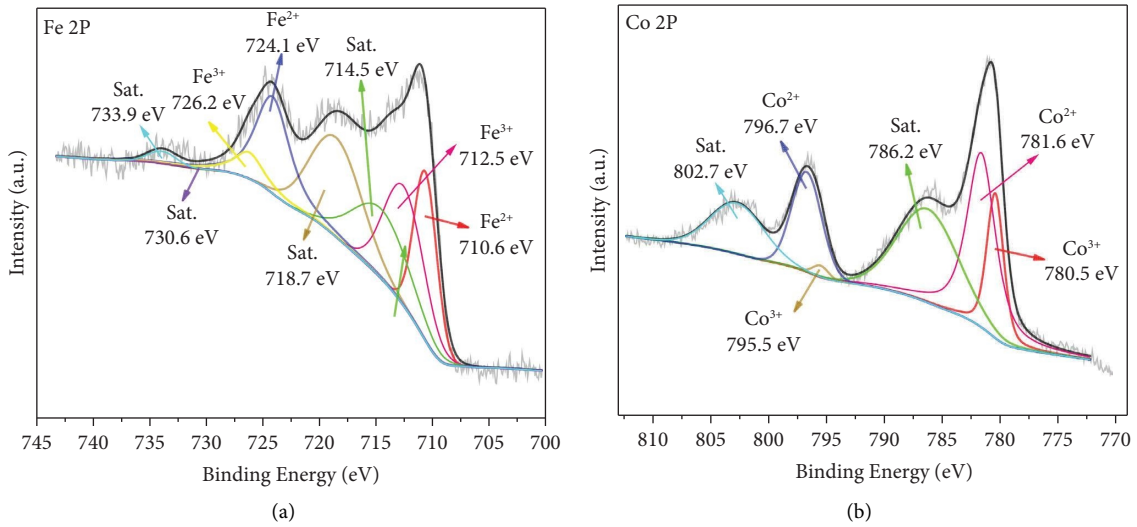

Figure 15: (a) XPS spectra of Fe 2p in used ZIF(Fe/Co)$_x$@CNF; (b) XPS spectra of Co 2p in used ZIF(Fe/Co)$_x$@CNF.

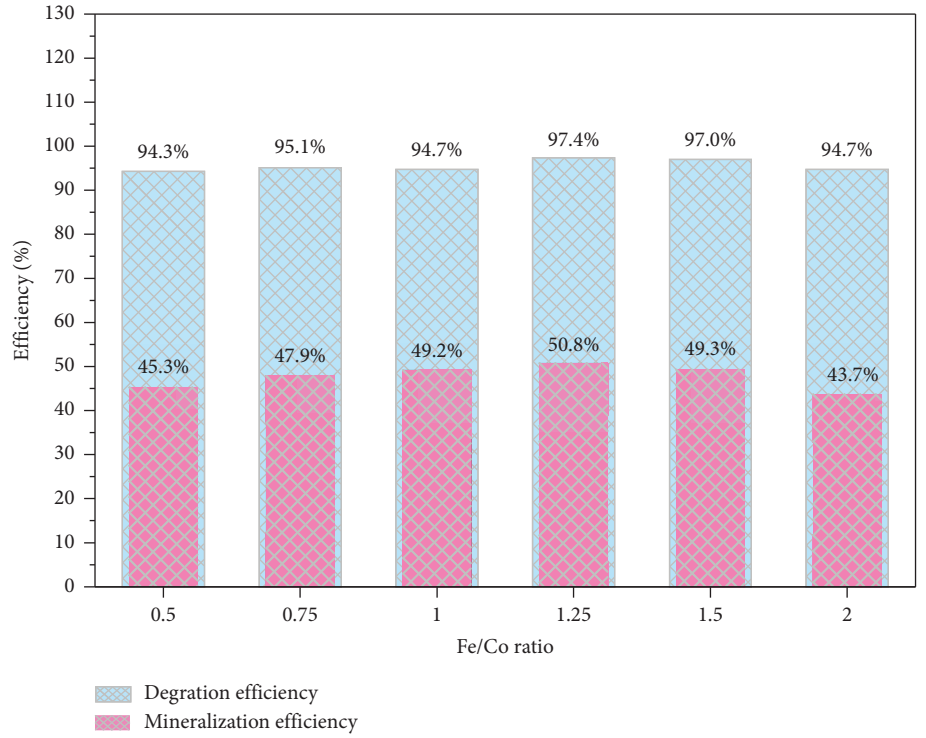

Figure 16: Mineralization rate of CEF degraded by ZIF(Fe/Co)$_x$@CNF with different Fe/Co ratios.

$$Fe^{3+} + e^- \longrightarrow Fe^{2+} + E^\theta = 0.771\,V \quad (18)$$

$$Co^{3+} + e^- \longrightarrow Co^{2+} + E^\theta = 1.808\,V \quad (19)$$

$$Fe^{2+} + HSO_5^- \longrightarrow Fe^{3+} + SO_4^{\bullet-} + OH^- \quad (20)$$

$$Fe^{3+} + HSO_5^- \longrightarrow Fe^{2+} + SO_5^{\bullet-} + H^+ \quad (21)$$

$$SO_4^{\bullet-} + OH^- \longrightarrow {\bullet}OH + SO_4^{2-} \quad (22)$$

$$Co^{2+} + HSO_5^- \longrightarrow Co^{3+} + SO_4^{\bullet-} + OH^- \quad (23)$$

$$Co^{3+} + HSO_5^- \longrightarrow Co^{2+} + SO_5^{\bullet-} + H^+ \quad (24)$$

$$Co^{3+} + Fe^{2+} \longrightarrow Co^{2+} + Fe^{3+} \quad (25)$$

Table 2: Catalytic properties of different materials.

Materials	Degrading efficiency (%)	k_{obs} (min^{-1})	TOC (%)
ZIF-67	81.3	0.085	32–34
Fe/Co-$ZIF_{1.0}$	91.4	0.101	37.6
Fe/Co-$ZIF_{1.25}$	91.4	0.105	38.4
Fe/Co-$ZIF_{1.5}$	88.7	0.091	32.9
Fe/Co-$ZIF_{1.0}$@CNF	93.3	0.126	43.2
Fe/Co-$ZIF_{1.25}$@CNF	94.0	0.135	43.8
Fe/Co-$ZIF_{1.5}$@CNF	85.8	0.098	42.2
ZIF$(Fe/Co)_{1.0}$@CNF	94.7	0.135	49.2
ZIF$(Fe/Co)_{1.25}$@CNF	97.4	0.151	50.8
ZIF$(Fe/Co)_{1.5}$@CNF	97.0	0.145	49.3

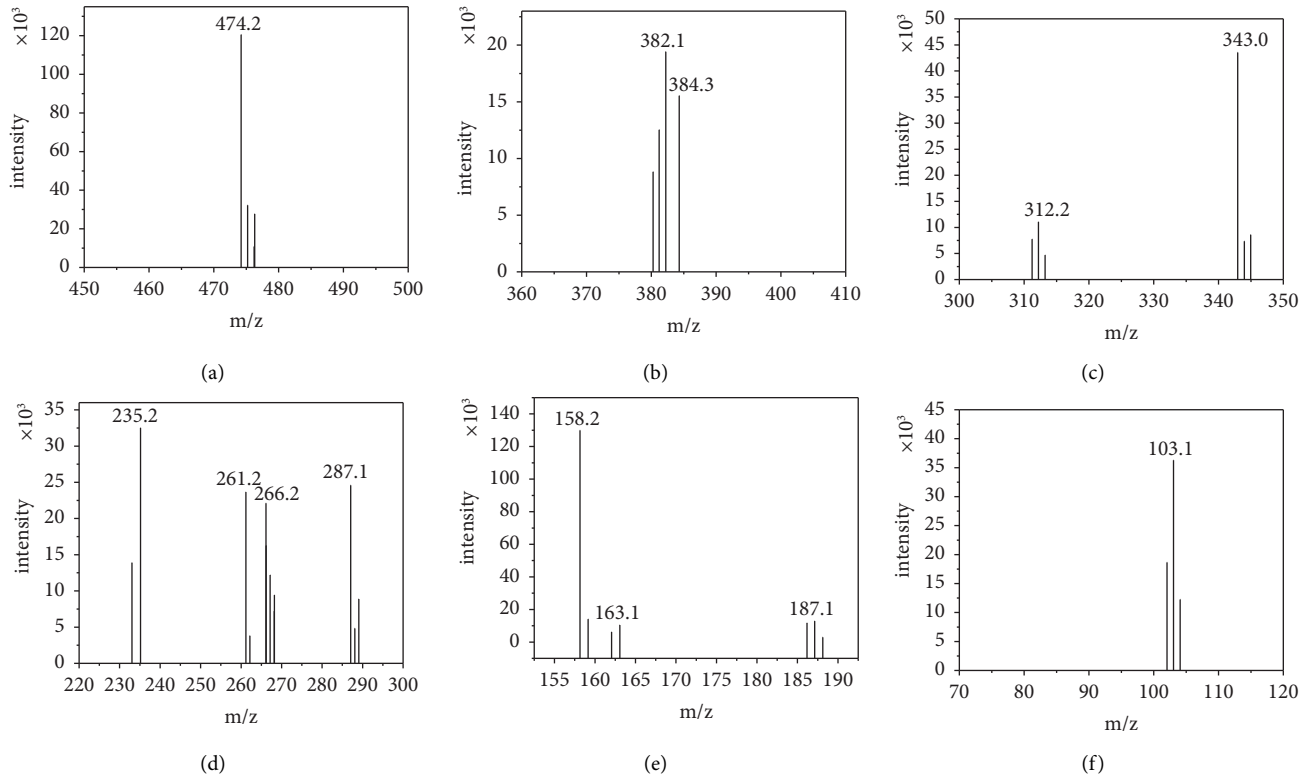

Figure 17: Mass spectra of intermediates.

3.4. Total Organic Carbon Test. To evaluate the mineralization effect of ZIF$(Fe/Co)_x$@CNF/PMS system on CEF degradation, the total organic carbon (TOC) removal rate was determined. As shown in Figure 16, the residual organic carbon content in the reaction solution was measured by the total organic carbon analyzer.

Clearly, the ZIF$(Fe/Co)_x$@CNF composite exhibited excellent catalytic performance and TOC mineralization rate. As shown in Figure 16, when the Fe/Co ratio of ZIF$(Fe/Co)_x$@CNF composite is 0.5 : 1 and 0.75 : 1, the TOC removal efficiency of ZIF$(Fe/Co)_x$@CNF/PMS for CEF is 45.3% and 47.9%, respectively. In addition, the TOC removal efficiency of ZIF$(Fe/Co)_x$@CNF/PMS system increased to 49.2% and 50.8% when the Fe/Co molar ratio of the ZIF$(Fe/Co)_x$@CNF is 1 : 1 and 1.25 : 1, respectively. This indicates that more than 50% of CEF is completely removed by appropriate Fe introduction.

Furthermore, in order to facilitate the comparison with ZIF-67, Fe/Co-ZIF, Fe/Co-ZIF@CNF, and explore the improvement of advanced oxidation properties of ZIF$(Fe/Co)_x$@CNF composites, the degradation efficiency of CEF, apparent rate constant k_{obs}, and total organic carbon removal rate of different Fe/Co molar ratio composites and other materials related to this study are listed in Table 2.

As can be seen from Table 2, ZIF$(Fe/Co)_x$@CNF prepared by Fe/Co-ZIF@CNF composite modified with 5,6-dimethyl benzimidazole has higher CEF degradation rate and reaction rate than ordinary ZIF-67 and Fe/Co-ZIF@CNF and has a higher TOC removal rate. When the Fe/Co molar ratio is 1.25 : 1, the catalytic performance of ZIF(Fe/

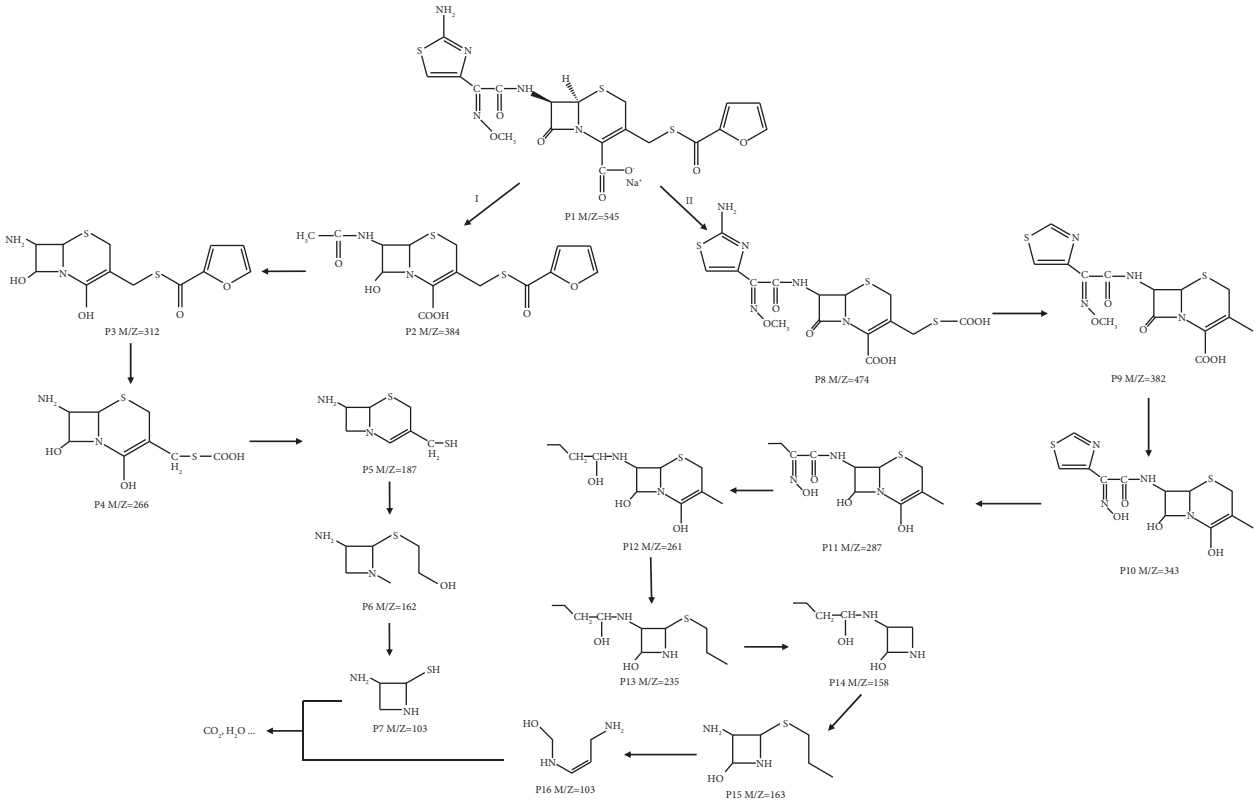

Figure 18: Possible degradation pathway of CEF by ZIF(Fe/Co)$_x$@CNF activation of PMS.

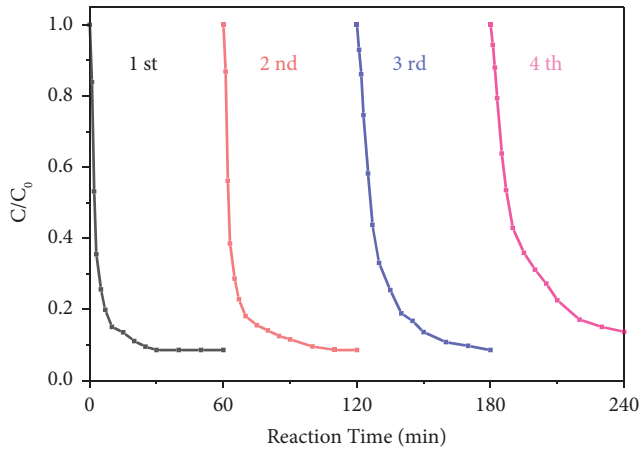

Figure 19: Degradation of CEF by ZIF(Fe/Co)$_x$@CNF/PMS system in three consecutive batches of experiments.

Co)$_{1.25}$@CNF is improved significantly. The degradation rate, k_{obs} value, and TOC removal rate of ZIF(Fe/Co)$_{1.25}$@CNF are up to 97.4%, 0.151 min^{-1}, and 50.8%, respectively. Compared with Fe/Co-ZIF@CNF, the catalytic performance of ZIF(Fe/Co)$_{1.25}$@CNF was significantly improved.

3.5. Possible Degradation Pathway. In order to reveal the degradation pathway of CEF in the ZIF(Fe/Co)$_x$@CNF/PMS reaction system, LC-MS was used to analyze the intermediates in the degradation process of CEF, the mass spectra of different intermediates were listed in Figure 17, and the possible degradation pathway was proposed. In addition to CEF itself, 15 possible intermediates were detected during the degradation process. Based on these intermediates and with reference to previous studies, two potential degradation pathways can be proposed.

As shown in Figure 18, the molecule at m/z = 545 represents CEF, consistent with its relative molecular mass. There are two pathways in CEF degradation. Mechanism I is shown as follows: by breaking the thioester bond, the five-membered heterocyclic ring in CEF cleaved to form the intermediate P2 (m/z = 384), followed by methyl and C=O bond cleaved to form the intermediate

P3 (m/z = 312). The -S-COOH in P4 is then attacked by the active substance to decarboxylate to form P5 (m/z = 187), which then opens the heterocyclic ring to form the intermediate P6 (m/z = 162). Finally, the S-C bond is broken to form the final product P7 (m/z = 103) as well as CO_2 and H_2O. Mechanism II can be described as follows: the five-membered carbon ring in CEF is opened by breaking the thioester bond, resulting in products P8 (m/z = 474), P1 to P8 (m/z = 264) similar to the process from P3 to P4. Then, the intermediate P9 (m/z = 382) was obtained by dehydration and decarboxylation with ammonia water. Next, due to the attack of SO4·−, two C-O single bonds are cleaved to the intermediate P10 (m/z = 343), which is then depyrrolization and defurylation to form the intermediate P11 (m/z = 287), and carbon reforming is performed. The process from P11 to P12 (m/z = 261) is mainly driven by oxidation reaction. Finally, the six-membered heterocyclic ring of P12 is broken, and the C-C bond is broken to form the final product P5 (m/z = 163) as well as CO_2 and H_2O.

3.6. Stability of ZIF(Fe/Co)$_x$@CNF in CEF Degradation. Although the prepared catalysts showed excellent catalytic activity, testing the reusability is important for their practical application. After the reaction, ZIF(Fe/Co)$_x$@CNF was removed from the reaction solution, washed, and dried with methanol and deionized water. And then, the washed and dried catalysts were reused for four more cycles under the same conditions. As shown in Figure 19, the CEF removal efficiency remained essentially unchanged in the first two cycles, and the CEF degradation rates were 97.4%, 94.9%, and 94.7% for the three consecutive cycles, indicating that ZIF(Fe/Co)$_x$@CNF showed good reusable potential activity. In the last cycle, the CEF degradation was found to decrease from 94.7% to 86.3%, reflecting the weak stability of ZIF(Fe/Co)$_x$@CNF after five cycles of reuse. It has been reported that during the reaction, contaminants may adsorb on the active sites of the catalyst, leading to the loss of catalytic activity [72]. In addition, the oxidation process resulted in a significant decrease in the Fe^{2+}/Fe^{3+} ratio, which would greatly affect the removal efficiency. The shedding of the bimetallic ZIF loaded on the carbon nanofibers after multiple cycles of ZIF(Fe/Co)$_x$@CNF may also be responsible for the decrease in the removal efficiency of CEF.

4. Conclusion

In this study, DMBIM-modified iron-doped cobalt zeolite imidazole skeletons were successfully prepared on carbon nanofibers. The Fe was uniformly distributed in the imidazole skeleton structure by hydrothermal process. Based on the synthesized materials with larger specific surface area, abundant porous structure, more stable properties than previous Fe/Co bimetallic ZIFs, and the synergistic effect between different components, ZIF(Fe/Co)$_x$@CNF exhibited 97.4% CEF degradation efficiency within 30 min. The mechanism of catalytic removal of CEF based on further studies, including the XPS technique, quenching experiments, and EPR tests, was postulated as follows:

(1) The ZIF(Fe/Co)$_x$@CNF/PMS system was found to be dominated by radicals, especially $SO_4^{\bullet-}$. In the reaction system, $SO_4^{\bullet-}$ dominates as the reactive radical, and no $^1O_2$ generated by the catalytic activation of PMS by ZIF(Fe/Co)$_x$@CNF was detected. Meanwhile, •OH affects the reaction only in a strongly basic environment with high pH. In contrast, $SO_4^{\bullet-}$ has a stronger redox potential, higher pH applicability range, and more stable mass transfer in some cases, resulting in the excellent catalytic efficiency of the reaction system.

(2) The synergistic effect of Co^{2+} and Fe^{2+} in the system was found to account for the excellent catalytic efficiency. Since the standard redox potential of Co^{3+}/Co^{2+} (1.808 V) is much higher than that of Fe^{3+}/Fe^{2+} (0.771 V), the abundant presence of Fe^{2+} in the ZIF(Fe/Co)$_x$@CNF material provided a convenient pathway for the capture of electrons by Co^{3+} and its rapid reconversion to Co^{2+}.

(3) Furthermore, when the Fe/Co molar ratio is 1.25 : 1, the catalytic performance of ZIF(Fe/Co)$_{1.25}$@CNF was improved significantly. The degradation rate, k_{obs} value, and TOC removal rate of ZIF(Fe/Co)$_{1.25}$@CNF are 97.4%, 0.151 min^{-1}, and 50.8%, respectively. This is a significant improvement over the ZIF-67. In addition, in four stability experiments, fresh and used ZIF(Fe/Co)^x@CNF showed no significant loss of catalytic activity, indicating that the introduction of CNF and DMBIM not only improved the degradation efficiency but also improved the stability of ZIF(Fe/Co)$_x$@CNF.

These observations suggest that ZIF(Fe/Co)$_x$@CNF provided a convenient strategy for the preparation of stable MOFs-derived materials with high catalytic activity, and the composites showed great potential for the effective treatment of refractory organics during the activation of SR-AOPs-based PMS.

Data Availability

The data used to support the findings of this study are included within the article.

Conflicts of Interest

The authors declare that they have no conflicts of interest.

Acknowledgments

The authors are grateful to the National Natural Science Foundation of China (No. 11805101 and No. 51908240); the Fundamental Research Funds for the Central Universities (No. 30921013110); the Provincial Ecological Environment Research Project of Jiangsu (No. 2022017); the Opening

Foundation of Key Laboratory for Palygorskite Science and Applied Technology of Jiangsu Province (No. HPK202001); the Open Fund by Jiangsu Key Laboratory of Atmospheric Environment Monitoring and Pollution Control (No. KHK2210).

References

[1] X. Liu, S. Lu, W. Guo, B. Xi, and W. Wang, "Antibiotics in the aquatic environments: a review of lakes, China," *Science of the Total Environment*, vol. 627, pp. 1195–1208, 2018.

[2] K. Reddersen, T. Heberer, and U. Dünnbier, "Identification and significance of phenazone drugs and their metabolites in ground-and drinking water," *Chemosphere*, vol. 49, no. 6, pp. 539–544, 2002.

[3] M. Kumar, S. Jaiswal, K. K. Sodhi et al., "Antibiotics bioremediation: perspectives on its ecotoxicity and resistance," *Environment International*, vol. 124, pp. 448–461, 2019.

[4] P. Grenni, V. Ancona, and A. Barra Caracciolo, "Ecological effects of antibiotics on natural ecosystems: a review," *Microchemical Journal*, vol. 136, pp. 25–39, 2018.

[5] B. Halling-Sørensen, S. Nors Nielsen, P. F. Lanzky, F. Ingerslev, H. Holten Lützhøft, and S. E. Jørgensen, "Occurrence, fate and effects of pharmaceutical substances in the environment-A review," *Chemosphere*, vol. 36, no. 2, pp. 357–393, 1998.

[6] K. Kümmerer, "Significance of antibiotics in the environment," *Journal of Antimicrobial Chemotherapy*, vol. 52, no. 1, pp. 5–7, 2003.

[7] Q.-Q. Zhang, G.-G. Ying, C.-G. Pan, Y.-S. Liu, and J.-L. Zhao, "Comprehensive evaluation of antibiotics emission and fate in the river basins of China: source analysis, multimedia modeling, and linkage to bacterial resistance," *Environmental Science and Technology*, vol. 49, no. 11, pp. 6772–6782, 2015.

[8] M. Bilal, S. S. Ashraf, D. Barceló, and H. M. N. Iqbal, "Biocatalytic degradation/redefining "removal" fate of pharmaceutically active compounds and antibiotics in the aquatic environment," *Science of the Total Environment*, vol. 691, pp. 1190–1211, 2019.

[9] H. Zhang, S. Lu, H. Ren et al., "Cytotoxicity and degradation product identification of thermally treated ceftiofur," *RSC Advances*, vol. 10, no. 31, pp. 18407–18417, 2020.

[10] A. B. A. Boxall, D. W. Kolpin, B. Halling-Sørensen, and J. Tolls, "Are veterinary medicines causing environmental risks?" *Environmental Science and Technology*, vol. 37, no. 15, pp. 286–294, 2003.

[11] R. Edirmanasinghe, R. Finley, E. J. Parmley et al., "A whole-genome sequencing approach to study cefoxitin-resistant*Salmonella enterica* serovar heidelberg isolates from various sources," *Antimicrobial Agents and Chemotherapy*, vol. 61, no. 4, Article ID e01919-16, 2017.

[12] M. Zeineldin, A. Megahed, B. Burton, B. Blair, B. Aldridge, and J. F. Lowe, "Effect of single dose of antimicrobial administration at birth on fecal microbiota development and prevalence of antimicrobial resistance genes in piglets," *Frontiers in Microbiology*, vol. 10, p. 1414, 2019.

[13] S. E. Ives and J. T. Richeson, "Use of antimicrobial metaphylaxis for the control of bovine respiratory disease in high-risk cattle," *Veterinary Clinics of North America: Food Animal Practice*, vol. 31, no. 3, pp. 341–350, 2015.

[14] R. Alexy, T. Kümpel, and K. Kümmerer, "Assessment of degradation of 18 antibiotics in the closed bottle test," *Chemosphere*, vol. 57, no. 6, pp. 505–512, 2004.

[15] J. Wang and S. Wang, "Preparation, modification and environmental application of biochar: a review," *Journal of Cleaner Production*, vol. 227, pp. 1002–1022, 2019.

[16] S. Zhuang, Y. Liu, and J. Wang, "Covalent organic frameworks as efficient adsorbent for sulfamerazine removal from aqueous solution," *Journal of Hazardous Materials*, vol. 383, Article ID 121126, 2020.

[17] J. Wang and S. Zhuang, "Removal of various pollutants from water and wastewater by modified chitosan adsorbents," *Critical Reviews in Environmental Science and Technology*, vol. 47, no. 23, pp. 2331–2386, 2017.

[18] S. Wang and J. Wang, "Activation of peroxymonosulfate by sludge-derived biochar for the degradation of triclosan in water and wastewater," *Chemical Engineering Journal*, vol. 356, pp. 350–358, 2019.

[19] R. Hernandez, M. Zappi, J. Colucci, and R. Jones, "Comparing the performance of various advanced oxidation processes for treatment of acetone contaminated water," *Journal of Hazardous Materials*, vol. 92, no. 1, pp. 33–50, 2002.

[20] J. Lee, U. von Gunten, and J.-H. Kim, "Persulfate-based advanced oxidation: critical assessment of opportunities and roadblocks," *Environmental Science and Technology*, vol. 54, no. 6, pp. 3064–3081, 2020.

[21] Z. Xiong, Y. Jiang, Z. Wu, G. Yao, and B. Lai, "Synthesis strategies and emerging mechanisms of metal-organic frameworks for sulfate radical-based advanced oxidation process: a review," *Chemical Engineering Journal*, vol. 421, Article ID 127863, 2021.

[22] M. Qi, P. Lin, Q. Shi, H. Bai, H. Zhang, and W. Zhu, "A metal-organic framework (MOF) and graphene oxide (GO) based peroxymonosulfate (PMS) activator applied in pollutant removal," *Process Safety and Environmental Protection*, vol. 171, pp. 847–858, 2023.

[23] F. Xie, Q. Shi, H. Bai et al., "An anode fabricated by Co electrodeposition on ZIF-8/CNTs/CF for peroxymonosulfate (PMS) activation," *Chemosphere*, vol. 313, Article ID 137384, 2023.

[24] M. Mahdi Ahmed, S. Barbati, P. Doumenq, and S. Chiron, "Sulfate radical anion oxidation of diclofenac and sulfamethoxazole for water decontamination," *Chemical Engineering Journal*, vol. 197, pp. 440–447, 2012.

[25] J. Li, W. Zhu, Y. Gao et al., "The catalyst derived from the sulfurized Co-doped metal–organic framework (MOF) for peroxymonosulfate (PMS) activation and its application to pollutant removal," *Separation and Purification Technology*, vol. 285, Article ID 120362, 2022.

[26] S. Wacławek, H. V. Lutze, K. Grübel, V. V. T. Padil, M. Černík, and D. D. Dionysiou, "Chemistry of persulfates in water and wastewater treatment: a review," *Chemical Engineering Journal*, vol. 330, pp. 44–62, 2017.

[27] L. J. Wang, H. Deng, H. Furukawa et al., "Synthesis and characterization of metal-organic framework-74 containing 2, 4, 6, 8, and 10 different metals," *Inorganic Chemistry*, vol. 53, no. 12, pp. 5881–5883, 2014.

[28] X. Zhang, J. Luo, K. Wan et al., "From rational design of a new bimetallic MOF family with tunable linkers to OER catalysts," *Journal of Materials Chemistry*, vol. 7, no. 4, pp. 1616–1628, 2019.

[29] A. Gu, P. Wang, K. Chen et al., "Core-shell bimetallic Fe-Co MOFs to activated peroxymonosulfate for efficient degradation of 2-chlorophenol," *Separation and Purification Technology*, vol. 298, Article ID 121461, 2022.

[30] X. Feng, S. Lin, M. Li, X. Bo, and L. Guo, "Comparative study of carbon fiber structure on the electrocatalytic performance

of ZIF-67," *Analytica Chimica Acta*, vol. 984, pp. 96–106, 2017.

[31] P. Pachfule, B. K. Balan, S. Kurungot, and R. Banerjee, "One-dimensional confinement of a nanosized metal organic framework in carbon nanofibers for improved gas adsorption," *Chemical Communications*, vol. 48, no. 14, pp. 2009–2011, 2012.

[32] X.-X. Xu, H.-Y. Yang, Z.-Y. Li, X.-X. Liu, and X.-L. Wang, "Loading of a coordination polymer nanobelt on a functional carbon fiber: a feasible strategy for visible-light-active and highly efficient coordination-polymer-based photocatalysts," *Chemistry - A European Journal*, vol. 21, no. 9, pp. 3821–3830, 2015.

[33] C. Hou, W. Chen, L. Fu, S. Zhang, C. Liang, and Y. Wang, "Facile synthesis of a Co/Fe bi-MOFs/CNF membrane nanocomposite and its application in the degradation of tetrabromobisphenol A," *Carbohydrate Polymers*, vol. 247, Article ID 116731, 2020.

[34] S. Yang, T. Xiao, J. Zhang, Y. Chen, and L. Li, "Activated carbon fiber as heterogeneous catalyst of peroxymonosulfate activation for efficient degradation of Acid Orange 7 in aqueous solution," *Separation and Purification Technology*, vol. 143, pp. 19–26, 2015.

[35] Z. Hu, Z. Guo, Z. Zhang, M. Dou, and F. Wang, "Bimetal zeolitic imidazolite framework-derived iron^{-}, cobalt^{-} and nitrogen-codoped carbon nanopolyhedra electrocatalyst for efficient oxygen reduction," *ACS Applied Materials & Interfaces*, vol. 10, no. 15, pp. 12651–12658, 2018.

[36] Q. Yang, S. Ren, Q. Zhao et al., "Selective separation of methyl orange from water using magnetic ZIF-67 composites," *Chemical Engineering Journal*, vol. 333, pp. 49–57, 2018.

[37] Y. Fei, M. Liang, L. Yan, Y. Chen, and H. Zou, "Co/C@cellulose nanofiber aerogel derived from metal-organic frameworks for highly efficient electromagnetic interference shielding," *Chemical Engineering Journal*, vol. 392, Article ID 124815, 2020.

[38] X. Sun, W. Xu, X. Zhang, T. Lei, S.-Y. Lee, and Q. Wu, "ZIF-67@Cellulose nanofiber hybrid membrane with controlled porosity for use as Li-ion battery separator," *Journal of Energy Chemistry*, vol. 52, pp. 170–180, 2021.

[39] M. M. Haafiz, A. Hassan, Z. Zakaria, and I. M. Inuwa, "Isolation and characterization of cellulose nanowhiskers from oil palm biomass microcrystalline cellulose," *Carbohydrate Polymers*, vol. 103, pp. 119–125, 2014.

[40] H. Yang, R. Yan, H. Chen, D. H. Lee, and C. Zheng, "Characteristics of hemicellulose, cellulose and lignin pyrolysis," *Fuel*, vol. 86, no. 12-13, pp. 1781–1788, 2007.

[41] X. Liu, Y. Li, Y. Ban et al., "Improvement of hydrothermal stability of zeolitic imidazolate frameworks," *Chemical Communications*, vol. 49, no. 80, pp. 9140–9142, 2013.

[42] S. K. Elsaidi, M. H. Mohamed, D. Banerjee, and P. K. Thallapally, "Flexibility in metal–organic frameworks: a fundamental understanding," *Coordination Chemistry Reviews*, vol. 358, pp. 125–152, 2018.

[43] A. L. Goodwin, K. W. Chapman, and C. J. Kepert, "Guest-dependent negative thermal expansion in nanoporous prussian blue analogues MIIPtIV(CN)$_6$·x{H_2O} ($0 \le x \le 2$; M = Zn, Cd)," *Journal of the American Chemical Society*, vol. 127, no. 51, pp. 17980-17981, 2005.

[44] J.-P. Zhang, H.-L. Zhou, D.-D. Zhou, P.-Q. Liao, and X.-M. Chen, "Controlling flexibility of metal–organic frameworks," *National Science Review*, vol. 5, no. 6, pp. 907–919, 2018.

[45] Y. Li, B. Jiang, and Y. Huang, "Constructing nanosheet-like MOF on the carbon fiber surfaces for improving the interfacial properties of carbo fiber/epoxy composites," *Applied Surface Science*, vol. 514, Article ID 145870, 2020.

[46] K.-Y. A. Lin, M.-T. Yang, J.-T. Lin, and Y. Du, "Cobalt ferrite nanoparticles supported on electrospun carbon fiber as a magnetic heterogeneous catalyst for activating peroxymonosulfate," *Chemosphere*, vol. 208, pp. 502–511, 2018.

[47] N. T. Thanh Tu, T. V. Thien, P. D. Du, V. T. Thanh Chau, T. X. Mau, and D. Q. Khieu, "Adsorptive removal of Congo red from aqueous solution using zeolitic imidazolate framework-67," *Journal of Environmental Chemical Engineering*, vol. 6, no. 2, pp. 2269–2280, 2018.

[48] Y. Zhou, Y. Zhang, and X. Hu, "Novel zero-valent Co-Fe encapsulated in nitrogen-doped porous carbon nanocomposites derived from $CoFe_2O_4$@ZIF-67 for boosting 4-chlorophenol removal via coupling peroxymonosulfate," *Journal of Colloid and Interface Science*, vol. 575, pp. 206–219, 2020.

[49] M.-P. Zhu, J.-C. E. Yang, X. Duan et al., "Interfacial $CoAl_2O_4$ from ZIF-67@γ-Al_2O_3 pellets toward catalytic activation of peroxymonosulfate for metronidazole removal," *Chemical Engineering Journal*, vol. 397, Article ID 125339, 2020.

[50] H. Wan, J. Yan, C. Guo, Q. Cui, and W. Zhang, "Synthesis of core-heteroshell structure for ZIF-67/VTM and its efficient activation of peroxymonosulfate in treatment of levofloxacin from an aqueous solution," *Environmental Research*, vol. 204, Article ID 111986, 2022.

[51] P. Lin, W. Zhu, Y. Gao et al., "Characteristics and mechanism of electrochemical peroxymonosulfate activation by a Co-N@CF anode for pollutant removal," *Environmental Sciences: Water Research and Technology*, vol. 8, no. 1, pp. 62–75, 2022.

[52] Y. Shang, C. Chen, P. Zhang et al., "Removal of sulfamethoxazole from water via activation of persulfate by Fe_3C@NCNTs including mechanism of radical and nonradical process," *Chemical Engineering Journal*, vol. 375, Article ID 122004, 2019.

[53] R. Ma, J. Liang, K. Takada, and T. Sasaki, "Topochemical synthesis of Co−Fe layered double hydroxides at varied Fe/Co ratios: unique intercalation of triiodide and its profound effect," *Journal of the American Chemical Society*, vol. 133, no. 3, pp. 613–620, 2011.

[54] Q. Yang, H. Choi, S. R. Al-Abed, and D. D. Dionysiou, "Iron-cobalt mixed oxide nanocatalysts: heterogeneous peroxymonosulfate activation, cobalt leaching, and ferromagnetic properties for environmental applications," *Applied Catalysis B-environmental*, vol. 88, no. 3-4, pp. 462–469, 2009.

[55] R. E. Huie and C. L. Clifton, "Rate constants for hydrogen abstraction reactions of the sulfate radical, SO_4^{-}. Alkanes and ethers," *International Journal of Chemical Kinetics*, vol. 21, no. 8, pp. 611–619, 1989.

[56] Q. Hu, J. Cao, Z. Yang et al., "Fabrication of Fe-doped cobalt zeolitic imidazolate framework derived from $Co(OH)_2$ for degradation of tetracycline via peroxymonosulfate activation," *Separation and Purification Technology*, vol. 259, Article ID 118059, 2021.

[57] J. W. T. Spinks and R. J. Woods, "An introduction to radiation chemistry," *Berichte der Bunsen-Gesellschaft Physical Chemistry Chemical Physics*, vol. 95, p. 451, 1990.

[58] W. Z. Tang and C. P. Huang, "2,4-Dichlorophenol oxidation kinetics by fenton's reagent," *Environmental Technology*, vol. 17, no. 12, pp. 1371–1378, 1996.

[59] S. Xin, G. Liu, X. Ma et al., "High efficiency heterogeneous Fenton-like catalyst biochar modified $CuFeO_2$ for the

degradation of tetracycline: economical synthesis, catalytic performance and mechanism," *Applied Catalysis B-environmental*, vol. 280, Article ID 119386, 2021.

[60] N. Lu, H. Lin, G. Li, J. Wang, Q. Han, and F. Liu, "ZIF-67 derived nanofibrous catalytic membranes for ultrafast removal of antibiotics under flow-through filtration via non-radical dominated pathway," *Journal of Membrane Science*, vol. 639, Article ID 119782, 2021.

[61] P. Neta, R. E. Huie, and A. B. Ross, "Rate constants for reactions of inorganic radicals in aqueous solution," *Journal of Physical and Chemical Reference Data*, vol. 17, no. 3, pp. 1027–1284, 1988.

[62] C. Liang and H.-W. Su, "Identification of sulfate and hydroxyl radicals in thermally activated persulfate," *Industrial and Engineering Chemistry Research*, vol. 48, no. 11, pp. 5558–5562, 2009.

[63] C. Qi, X. Liu, J. Ma, C. Lin, X. Li, and H. Zhang, "Activation of peroxymonosulfate by base: implications for the degradation of organic pollutants," *Chemosphere*, vol. 151, pp. 280–288, 2016.

[64] W. Adam, D. V. Kazakov, and V. P. Kazakov, "Singlet-oxygen chemiluminescence in peroxide reactions," *Chemical Reviews*, vol. 105, no. 9, pp. 3371–3387, 2005.

[65] F. Xie, W. Zhu, P. Lin et al., "A bimetallic (Co/Fe) modified nickel foam (NF) anode as the peroxymonosulfate (PMS) activator: characteristics and mechanism," *Separation and Purification Technology*, vol. 296, Article ID 121429, 2022.

[66] P. Duan, T. Ma, Y. Yue et al., "Fe/Mn nanoparticles encapsulated in nitrogen-doped carbon nanotubes as a peroxymonosulfate activator for acetamiprid degradation," *Environmental Science-nano*, vol. 6, no. 6, pp. 1799–1811, 2019.

[67] M. Nie, Y. Yang, Z. Zhang et al., "Degradation of chloramphenicol by thermally activated persulfate in aqueous solution," *Chemical Engineering Journal*, vol. 246, pp. 373–382, 2014.

[68] J. Chen, L. Zhang, T. Huang, W. Li, Y. Wang, and Z. Wang, "Decolorization of azo dye by peroxymonosulfate activated by carbon nanotube: radical versus non-radical mechanism," *Journal of Hazardous Materials*, vol. 320, pp. 571–580, 2016.

[69] Z. Wang, R. Yuan, Y. Guo, L. Xu, and J. Liu, "Effects of chloride ions on bleaching of azo dyes by Co^{2+}/oxone regent: kinetic analysis," *Journal of Hazardous Materials*, vol. 190, no. 1-3, pp. 1083–1087, 2011.

[70] W. Zhang, S. Zhou, J. Sun et al., "Impact of chloride ions on UV/H_2O_2 and UV/persulfate advanced oxidation processes," *Environmental Science and Technology*, vol. 52, no. 13, pp. 7380–7389, 2018.

[71] F. Chen, L.-L. Liu, J.-J. Chen et al., "Efficient decontamination of organic pollutants under high salinity conditions by a nonradical peroxymonosulfate activation system," *Water Research*, vol. 191, Article ID 116799, 2021.

[72] Z. Wu, Y. Wang, Z. Xiong et al., "Core-shell magnetic Fe_3O_4@Zn/Co-ZIFs to activate peroxymonosulfate for highly efficient degradation of carbamazepine," *Applied Catalysis B-environmental*, vol. 277, Article ID 119136, 2020.

[73] L. Lai, H. Ji, H. Zhang et al., "Activation of peroxydisulfate by V-Fe concentrate ore for enhanced degradation of carbamazepine: surface ≡V(III) and ≡V(IV) as electron donors promoted the regeneration of ≡Fe(II)," *Applied Catalysis B-environmental*, vol. 282, 2021.

[74] J. Li, M. Xu, G. Yao, and B. Lai, "Enhancement of the degradation of atrazine through $CoFe_2O_4$ activated peroxymonosulfate (PMS) process: kinetic, degradation intermediates, and toxicity evaluation," *Chemical Engineering Journal*, vol. 348, pp. 1012–1024, 2018.

[75] Y. Xu, H. Lin, Y. Li, and H. Zhang, "The mechanism and efficiency of MnO_2 activated persulfate process coupled with electrolysis," *Science of the Total Environment*, vol. 609, pp. 644–654, 2017.

[76] X. Lou, L. Wu, Y. Guo et al., "Peroxymonosulfate activation by phosphate anion for organics degradation in water," *Chemosphere*, vol. 117, pp. 582–585, 2014.

[77] G. V. Buxton, C. L. Greenstock, W. P. Helman, and A. B. Ross, "Critical Review of rate constants for reactions of hydrated electrons, hydrogen atoms and hydroxyl radicals (·OH/·O^- in Aqueous Solution," *Journal of Physical and Chemical Reference Data*, vol. 17, no. 2, pp. 513–886, 1988.

[78] M. Zhang, C. Xiao, X. Yan et al., "Efficient removal of organic pollutants by metal-organic framework derived Co/C yolk-shell nanoreactors: size-exclusion and confinement effect," *Environmental Science and Technology*, vol. 54, no. 16, pp. 10289–10300, 2020.

[79] Y. Zhou, J. Jiang, Y. Gao et al., "Activation of peroxymonosulfate by benzoquinone: a novel nonradical oxidation process," *Environmental Science and Technology*, vol. 49, no. 21, pp. 12941–12950, 2015.

[80] Z. Zhu, C. Ji, L. Zhong et al., "Magnetic Fe-Co crystal doped hierarchical porous carbon fibers for removal of organic pollutants," *Journal of Materials Chemistry*, vol. 5, no. 34, pp. 18071–18080, 2017.

[81] P. Hu and M. Long, "Cobalt-catalyzed sulfate radical-based advanced oxidation: a review on heterogeneous catalysts and applications," *Applied Catalysis B-environmental*, vol. 181, pp. 103–117, 2016.

[82] H. Chen, Y. Liu, T. Cai et al., "Boosting photocatalytic performance in mixed-valence MIL-53(Fe) by changing Fe^{II}/Fe^{III} ratio," *ACS Applied Materials & Interfaces*, vol. 11, no. 32, pp. 28791–28800, 2019.

[83] P. Liang, C. Zhang, X. Duan et al., "N-doped graphene from metal-organic frameworks for catalytic oxidation of p-hydroxylbenzoic acid: N-functionality and mechanism," *ACS Sustainable Chemistry & Engineering*, vol. 5, no. 3, pp. 2693–2701, 2017.